Monthly Notices
of the
ROYAL ASTRONOMICAL SOCIETY

MNRAS **482,** 2750–2769 (2019)
Advance Access publication 2018 October 23

doi:10.1093/mnras/sty2870

Signatures of an eruptive phase before the explosion of the peculiar core-collapse SN 2013gc

Andrea Reguitti [1]★ A. Pastorello,[2] G. Pignata,[3,4] S. Benetti,[2] E. Cappellaro,[2] M. Turatto,[2] C. Agliozzo [3,4] F. Bufano,[5] N. I. Morrell,[6] F. Olivares E.,[3,4] D. E. Reichart,[7] J. B. Haislip,[7] V. Kouprianov,[7] S. J. Smartt[8] and S. Ciroi[1]

[1]*Dipartimento di Fisica e Astronomia 'G. Galilei', Università di Padova, Vicolo dell'Osservatorio 3, I-35122 Padova, Italy*
[2]*INAF – Osservatorio Astronomico di Padova, Vicolo dell'Osservatorio 5, I-35122 Padova, Italy*
[3]*Departamento de Ciencias Físicas – Universidad Andrés Bello, Avda. República 252, Santiago, 8320000 Chile*
[4]*Millennium Institute of Astrophysics, Nuncio Monsenor Sótero Sanz 100, Providencia, Santiago, 8320000 Chile*
[5]*INAF – Osservatorio Astrofisico di Catania, Via S. Sofia 78, I-95123 Catania, Italy*
[6]*Las Campanas Observatory, Carnegie Observatories, Casilla 601, La Serena, 1700000 Chile*
[7]*Department of Physics and Astronomy, University of North Carolina at Chapel Hill, Campus Box 3255, Chapel Hill, NC 27599, USA*
[8]*Astrophysics Research Centre, School of Mathematics and Physics, Queen's University Belfast, Belfast, BT7 1NN, UK*

Accepted 2018 October 21. Received 2018 September 27; in original form 2018 June 21

ABSTRACT

We present photometric and spectroscopic analysis of the peculiar core-collapse supernova (SN) 2013gc, spanning 7 yr of observations. The light curve shows an early maximum followed by a fast decline and a phase of almost constant luminosity. At +200 d from maximum, a brightening of 1 mag is observed in all bands, followed by a steep linear luminosity decline after +300 d. In archival images taken between 1.5 and 2.5 yr before the explosion, a weak source is visible at the supernova location, with mag ≈20. The early supernova spectra show Balmer lines, with a narrow (∼560 km s^{-1}) P-Cygni absorption superimposed on a broad (∼3400 km s^{-1}) component, typical of Type IIn events. Through a comparison of colour curves, absolute light curves, and spectra of SN 2013gc with a sample of supernovae IIn, we conclude that SN 2013gc is a member of the so-called Type IId subgroup. The complex profile of the Hα line suggests a composite circumstellar medium geometry, with a combination of lower velocity, spherically symmetric gas, and a more rapidly expanding bilobed feature. This circumstellar medium distribution has been likely formed through major mass-loss events that we directly observed from 3 yr before the explosion. The modest luminosity ($M_{\rm I} \sim -16.5$ near maximum) of SN 2013gc at all phases, the very small amount of ejected ^{56}Ni (of the order of 10^{-3} M$_\odot$), the major pre-supernova stellar activity, and the lack of prominent [O I] lines in the late-time spectra support a fall-back core-collapse scenario for the massive progenitor of SN 2013gc.

Key words: supernovae: general – supernovae: individual: SN 2013gc, SN 1994aj, SN1996al, SN1996L, SN2000P.

1 INTRODUCTION

Major astronomical surveys, such as the Asteroid Terrestrial-impact Last Alert System (ATLAS; Tonry et al. 2018), the All Sky Automated Survey for SuperNovae (ASAS-SN; Shappee et al. 2014), and the Panoramic Survey Telescope and Rapid Response System (Pan-STARRS; Chambers et al. 2016), are discovering a growing number of peculiar stellar transients that display a wide range of photometric and spectroscopic properties. A fraction of them show supernova (SN) features, with high-velocity gas. Some also exhibit signatures of interaction between fast-moving ejecta and the circumstellar medium (CSM), which is revealed through multi-component line profiles in the spectra. In particular, SNe showing narrow H emission lines likely produced in the unshocked photoionized gas (Chevalier & Fransson 1994; Chugai & Danziger 1994) are classified as Type IIn (Schlegel 1990). A well-studied member of this class is SN 1988Z (Stathakis & Sadler 1991; Turatto et al. 1993; Aretxaga et al. 1999; Smith et al. 2017).

A dense, H-rich CSM is generally produced through mass-loss events from the progenitor star that occurred from tens to thousands of years before the SN explosion (Smith 2014). However, in some

★ E-mail: andrea.reguitti@studenti.unipd.it

cases, the H-rich CSM grows through eruptive episodes that occurred a short time (e.g. a few months to years) before the terminal stellar death. The energetics of these pre-SN outbursts is quite high (10^{48} 10^{49} erg), and the ejected gas moves at a speed of tens to $\lesssim 10^3$ km s^{-1}. In contrast, fast-moving SN ejecta have velocities of several thousand km s^{-1}.

The photometric evolution of SNe IIn is different from that of normal Type II SNe. The recombination of the CSM photoionized by the shock breakout gives an additional source of energy, powering the very early light curve of the SN. The subsequent interaction between SN ejecta and the CSM converts the kinetic energy of the shock wave into radiation. This is a more efficient powering mechanism, allowing the luminosity to remain almost constant. In some cases, the light curve may even show a brightening. This source of energy is additive to the ^{56}Ni/^{56}Co decays, and the SN remains visible even for years after the explosion (Milisavljevic et al. 2012; Benetti et al. 2016).

The variety of observational properties of SNe IIn depends on the velocity of the different gas components, their chemical composition and geometry, the mass-loss history, and consequently the CSM density profile (Chugai 1997). Their spectra are characterized by strong emission lines of the Balmer series superposed on a rather blue continuum, with Hα being the most prominent feature. The profile of these lines is complex, including a broad shallow component, on top of which the characteristic narrow line sits. The velocities inferred from the full width at half-maximum (FWHM) of the two components are typically several thousand (sometimes exceeding 10^4) and a few hundred km s^{-1}, respectively. In some cases a blueshifted narrow P-Cygni absorption is also present. A third component, with intermediate width, can also be observed with a velocity of several hundred to a few thousand km s^{-1}. The Hα line dominates the spectra at all phases, including at late times, when the blue continuum becomes redder or eventually disappears.

Different types of massive core-collapse SN progenitors are known to experience severe mass loss during their late evolutionary phases, including events triggered by major outbursts. Luminous and massive stars, including hypergiants and red supergiants, may lose mass through strong stellar winds during their evolution, or via binary interaction. In particular, luminous blue variables (LBVs) occasionally produce a spectacular giant eruption (GE), during which they lose a considerable amount of material (up to tens of solar masses). The best followed GE of an LBV in the Milky Way was that of η Carinae in the mid-19th century. It lasted a few decades, during which the star grew its luminosity up to absolute magnitude $M \sim -14$ (Smith & Frew 2011). An LBV GE that occurs in a distant galaxy can be confused with an underluminous Type IIn SN. For this reason, extragalactic GEs (or major outbursts) of hypergiants are sometimes dubbed as 'SN Impostors' (Van Dyk et al. 2000).

LBVs may exhibit an extreme variability, with oscillations exceeding 5 mag, over periods of many years. These outbursts sometimes are premonitions of subsequent Type II SN explosions. This was directly observed in SN 2009ip (Mauerhan et al. 2013; Smith, Mauerhan & Prieto 2014); LSQ13zm (Tartaglia et al. 2016), SN 2016bdu (Pastorello et al. 2018); and SNhunt151 (Elias-Rosa et al. 2018). The progenitor of SN 2009ip had a non-terminal outburst in 2009. Other outbursts of the same object were observed in the following years, until a much brighter event occurred in summer 2012, which was claimed to be the signature of the final core collapse. Whether the 2012 event was a real SN or a non-terminal explosion is still controversial (Pastorello et al. 2013; Margutti et al. 2014). The sequence of events observed in SN 2009ip indicated that the progenitor was likely an LBV. Multiple outbursts accompanied by major mass loss allow the formation of a dense H-rich cocoon around the star. Hence, when the star finally exploded, it showed up as a Type IIn SN.

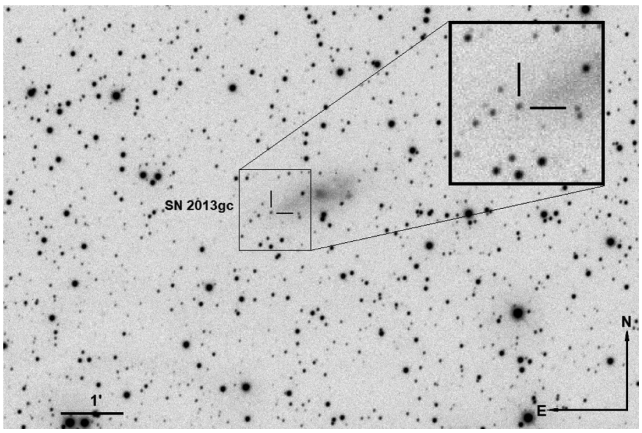

Figure 1. Discovery image of SN 2013gc taken on 2013 November 7 with the PROMPT-3 telescope and clear filter. A blow up of the SN location is shown in the top-right inset.

In the vast array of displays of SNe IIn, a group exhibits peculiar 'double' (broad and narrow) P-Cygni profile in the H lines, signatures of the SN ejecta and CSM, respectively. For this spectral property, these peculiar Type IIn events are labelled as 'Type IId' (see the review of Benetti 2000). This category includes SN 1994aj (Benetti et al. 1998), SN 1996L (Benetti et al. 1999), and SN 1996al (Benetti et al. 2016). These objects are quite rare, and this paper discusses the case of a possible new member, SN 2013gc.

The structure of the paper is as follows: We introduce the discovery of SN 2013gc, the physical properties of the host galaxy, including a discussion of the reddening and the distance, in Section 2. Information of the instrumentation used and a description of the data reduction techniques are reported in Section 3. An analysis of the light curve is provided in Section 4, while in Section 5 we analyse the reddening-corrected colour and absolute magnitude curves. In Section 6 we present robust evidence of progenitor variability before the explosion. The spectral features and evolution of the Hα profile are discussed in Section 7. A discussion of the progenitor and the physics of the explosion is presented in Section 8. Finally, the conclusions are summarized in Section 9. In Appendix A, we present the photometric measurements and the spectra of another SN IIn/IId 2000P, which has been used as a comparison object in this paper.

2 DISCOVERY

SN 2013gc (= PSN J08071188−2803263) was discovered on 2013 November 7 at RA = $08^{\rm h}07^{\rm m}11\overset{\rm s}{.}88$ and Dec.= $-28^\circ03'26\overset{''}{.}32$ (J2000), 43.3 arcsec east and 18.0 arcsec south of the nucleus of the galaxy ESO 430-20 (a.k.a. PGC 22788; Antezana et al. 2013). The discovery chart is in Fig. 1. The discovery was done by the CHilean Automatic Supernova sEarch survey (CHASE; Pignata et al. 2009), using the Panchromatic Robotic Optical Monitoring and Polarimetry Telescopes (PROMPT; Reichart et al. 2005), at the Cerro Tololo Inter-American Observatory (CTIO).

The original spectral classification indicated it was an Sn IIn (Antezana et al. 2013). The spectrum, discussed in Section 7, was obtained soon after the discovery with the Las Campanas 2.5-m du Pont telescope (+WFCCD), and cross-correlated with a library

Table 1. Properties of ESO 430-20.

α (J2000)	$08^{h}07^{m}08\overset{s}{.}6$
δ (J2000)	$-28^{\circ}03'08\overset{''}{.}8$
Morphological type	SAB(s)d
Diameter[a]	1.90×0.78 arcmin
Redshift[a]	$0.003\,402 \pm 0.000\,007$
v_{Hel}[a]	1020 ± 2 km s^{-1}
$v_{Virgo+GA+Shapley}$[b]	942 ± 20 km s^{-1}
Distance modulus[c]	30.46 ± 0.19
A_V	1.253 mag

Notes. [a]Theureau et al. (1998).
[b]Mould et al. (2000).
[c]Adopted.

of SN spectra using the 'Supernova Identification' code (SNID; Blondin & Tonry 2007). SN 2013gc appeared as a Type IIn SN similar to SN 1996L (Benetti et al. 1999) at about two months after the explosion.

2.1 The SN environment

The host galaxy ESO 430-20 is a member of a small group of galaxies (Crook et al. 2007). The morphological classification, from the RC3 Catalogue (De Vaucouleurs et al. 1991), is SAB(s)d. Details on the host galaxy obtained from the NASA/IPAC Extragalactic Database (NED)[1] are summarized in Table 1. The Type II SN 2013ak was also discovered in this galaxy, on 2013 March 9 (Carrasco et al. 2013), at a magnitude of 13.5. The location of SN 2013gc is far from the galaxy centre: With a distance of 12.37 Mpc, the SN is 2.81 kpc from the nucleus, while the radius of the galaxy is 3.4 kpc. Due to the relatively large radial distance from the galaxy centre, the local dust contamination is likely small.

2.2 Distance

The distance of ESO 430-20 is controversial. The Virgo + Great Attractor + Shapley velocity ($v = 942 \pm 20$ km s^{-1}, Table 1), assuming $H_0 = 73$ km s^{-1} Mpc^{-1}, provides a distance $d = 12.90 \pm 0.27$ Mpc, hence $\mu = 30.55 \pm 0.05$ mag. Crook et al. (2007) determined a distance of 13.36 Mpc, equal to $\mu = 30.63$ mag. The HyperLeda catalogue reports a radial velocity corrected for Virgo Cluster infall $V_{Vir} = 793 \pm 2$ km s^{-1}, hence a distance $d = 12.0^{+10.6}_{-5.6}$ Mpc and $\mu = 30.40 \pm 1.37$ mag.

Theureau et al. (2007) gave three different distance estimates of the host galaxy through photometry in three near-infrared (NIR) bands and applying the Tully–Fisher (TF) relation: $d = 11.4$ Mpc in J, $d = 11.5$ Mpc in H, and $d = 12$ Mpc in K, with μ of 30.29 ± 0.46, 30.31 ± 0.47, and 30.40 ± 0.45 mag, respectively.

More recently, Tully, Courtois & Sorce (2016) estimated $d = 6.95$ Mpc for ESO 430-20, corresponding to $\mu = 29.21 \pm 0.54$ mag, obtained from the TF relation, calibrated on a sample of galaxy clusters. The discrepancy with the previous determinations is very large, so we do not take into account this result in the choice of the distance to adopt.

For the distance, the mean of the three TF determinations obtained by Theureau et al. (2007), and the two kinematical velocities reported in Table 1, are considered. We hence adopt $d = 12.37 \pm 1.07$ Mpc and $\mu = 30.46 \pm 0.19$ mag throughout this paper.

[1]http://ned.ipac.caltech.edu/

2.3 Reddening

The Galactic reddening A_V reported in Table 1 is from Schlafly & Finkbeiner (2011). Assuming $R_V = 3.1$ (Fitzpatrick 1999), a colour excess $E(B - V) = 0.404$ mag is derived. We adopt the Cardelli, Clayton & Mathis (1989) extinction law. The extinction is quite large due to the low Galactic latitude of the galaxy ($\sim 2.3^{\circ}$). This makes the reddening value very uncertain. We warn that the inaccuracy of the Schlafly extinction maps can lead to inaccuracy on the intrinsic distance and absolute magnitude of the object.

On the other hand, we are not able to estimate the internal reddening of the host galaxy. We notice that the spectra do not show the narrow Na ID doublet features at the redshift of the host galaxy, because of the modest flux of the continuum at these wavelengths. The host galaxy reddening is hence assumed to be negligible, which is consistent with the remote location of the SN in the host galaxy.

3 SET-UP AND DATA REDUCTION

Johnson–Cousins *BVRIJHK*, Sloan *grizy*, and unfiltered photometric images were obtained from a large number of observing facilities, whose technical notes are summarized here. For the photometry, we used

(i) The PROMPT facility, located at CTIO, which consists of six 0.41-m robotic telescopes (Reichart et al. 2005).[2]

(ii) The TRAnsiting Planets and PlanetesImals Small Telescope (TRAPPIST), which is a robotic 0.5-m Ritchey–Chrétien telescope located at ESO La Silla Observatory.[3]

(iii) The NTT telescope at La Silla, equipped with the ESO Faint Object Spectrograph and Camera (EFOSC2)[4] and the Son of Isaac (SOFI).[5]

(iv) The Southeastern Association for Research in Astronomy (SARA), which is a consortium of colleges that operates some remote facilities, including a 0.6-m telescope[6] on Cerro Tololo, in Chile.

(v) The SMARTS 1.3-m CTIO telescope, with the ANDICAM detector.[7]

(vi) The Gemini-South 8.1-m telescope at Cerro Pachón, with the GMOS instrument.[8]

(vii) The 1.2-m 'S. Oschin' Schmidt telescope at Palomar Observatory, during the Palomar Transient Factory (PTF) survey.[9] These

[2]The optical imagers, made by Apogee, use back-illuminated E2V 1024 × 1024 CCDs, with a 10 arcmin field of view and a pixel scale of 0.6 arcmin per pixel.
[3]The telescope is equipped with a Fairchild 3041 back-illuminated 2k × 2k CCD. The pixel scale is 0.64 arcmin per pixel; the field of view is 22 ×22 arcmin.
[4]The detector of the instrument is a thin CCD with 2048 × 2048 pixels and a pixel size of 0.12 arcmin.
[5]This is a NIR spectrograph and imaging camera, with a HgCdTe 1024 × 1024 pixel detector.
[6]The instrument is equipped with a 2048 × 2048 pixel E2V CCD. The pixel scale is 0.44 arcmin per pixel, with an FOV of 15 arcmin. The filter set includes Johnson *UBVRI* and *SDSS ugriz*.
[7]Two instruments can perform optical and NIR images. The CCD is 1024 × 1024 pixels wide, and has a pixel scale of 0.371 arcmin per pixel.
[8]The instrument is an imager, long-slit and multislit spectrograph, with an FOV of over 5.5 square arcminutes. It is equipped with an EEV CCD, with a pixel scale of 0.08 arcmin per pixel.
[9]The survey is performed with a 12k × 8k CCD mosaic. The pixel scale is 0.1 arcmin per pixel.

data were retrieved through the web interface http://irsa.ipac.caltech.edu/applications/ptf/.

(viii) The 1.8-m telescope on Haleakala, Hawaii, during the Pan-STARRS 1 (PS1) survey (Chambers et al. 2016; Magnier et al. 2016), with the Gigapixel Camera 1 (GPC1).[10]

(ix) The European Southern Observatory (ESO) 2.6-m Very Large Telescope (VLT) Survey Telescope (VST) at Cerro Paranal, with OMEGACAM. The camera is composed with a mosaic of 32 2k × 4k pixel CCDs, with a total of 268 megapixels and a field of view (FOV) of 1 square degree. The pixel scale is 0.215 arcsec per pixel.

3.1 Data reduction

For the photometric data reduction we used a dedicated pipeline called SNOOPY[11] (Cappellaro 2014).

The optical images were corrected for bias, overscan, and flat-field, using standard IRAF tasks. If several dithered exposures with the same instrumental configuration were taken on the same night, they were combined to increase the signal-to-noise ratio (SNR). The SNOOPY package was used for astrometric calibration and seeing determination on the images. The point spread function (PSF)-fitting technique was used to determine the instrumental SN magnitude. For each image, we built a PSF model using the profiles of bright, isolated stars in the field. We subtracted the sky background fitting a low-order polynomial (typically a second-order). Then, the modelled source was subtracted from the original frames, a new estimate of the local background was performed, and the fitting procedure was repeated. If the source was not detected, an upper limit to the luminosity was established.

Photometric nights were used to calibrate the magnitudes of reference stars in the SN field, through the observations of Landolt (1992) standard fields with the same instrumental set-up. This local sequence was used to correct the instrumental zero-points on non-photometric nights. Photometric errors were estimated through artificial star experiments, combined in quadrature with the uncertainties derived from the PSF fitting returned by DAOPHOT. Finally, we calibrated the final instrumental magnitudes of the SN in the Johnson–Cousins and Sloan photometric systems, using differential photometry. For the calibration of the PS1 survey images, we followed the prescriptions of Magnier et al. (2016).

The few Sloan *r* and *i* (apart from those of the PS1 survey) magnitudes were transformed in the Johnson–Cousins photometric system following the equations of Chonis & Gaskell (2008). Clear filter magnitudes from PROMPT were treated as Cousins *R*-band magnitudes, because the wavelength efficiency peak of the detector is similar to that of the *R* filter response curve.

Only a single epoch of *J*, *H*, and *K* imaging of the SN, along with a few additional NIR frames of the SN field taken before the explosion, is available. Clean sky images were obtained by median-combining multiple dithered images of the field, and consequently subtracted to individual images. Sky-subtracted images were finally combined to increase the SNR. PSF-fitting photometry was also performed on the NIR sources, and the final SN magnitudes were calibrated using the 2MASS catalogue as reference.

[10]The camera is composed of an array of 60 back-illuminated CCDs, with a 7 square degrees FOV. The pixel scale is 0.258 arcmin per pixel. The survey is performed with *grizy* filters.

[11]SNOOPY is a package for SN photometry using PSF fitting and/or template subtraction developed by E. Cappellaro. A package description can be found at http://sngroup.oapd.inaf.it/snoopy.html.

4 LIGHT CURVE

Our photometric follow-up campaign of SN 2013gc spans 7 yr, starting from March 2010. The first detection of the SN is on 2013 August 26, ∼1.5 months before the discovery announcement. With only one observation during the rising phase, it is not possible to precisely determine the explosion epoch. The last non-detection is dated 2013 June 19; hence, the SN must have exploded between the above two dates. As we will detail in Section 8, we assume 2013 August 16 (MJD 56520) as the explosion date. The object has been followed for about 2 yr, up to June 2015. Pre-explosion images and those obtained at very late phases are unfiltered. For SN 2000P, the multiband magnitudes are reported in Table A1 and Table A2. For SN 2013gc, the optical magnitudes are reported in Table A3 and the infrared in Table A4, while unfiltered magnitudes are listed in Table A5.

The photometric coverage of the SN evolution in the *BVRIJHK* and *gzy* bands is shown in Fig. 2. Magnitudes are not corrected for the line-of-sight extinction. We assume MJD 56544 ± 7 as an indicative epoch for the maximum luminosity, that is 4 d before the brightest *V*-band magnitude (MJD 56548) and 20 d before the brightest point in the *I* band (MJD 56564). This agrees with the estimate of Antezana et al. (2013).

The light curve shows a fast linear decline after maximum, with a rate of 6.6 ± 0.2, 7.5 ± 0.3, and 6.1 ± 0.2 mag (100 d)$^{-1}$ in the *V*, *R*, and *I* bands, respectively. Such decline rates are typical of the 'linear' subclass of Type II SNe (Valenti et al. 2016). Two EFOSC2 observations have been performed 3 and 4 d after our estimated maximum, when the SN was at $V = 15.1$ mag (hence, $M_V \sim -16.6$ mag).

The initial linear decline is followed by a slower decline in all bands. This phase, lasting ∼20 d, is well sampled in the *R* band with a slope of 1.02 ± 0.11 mag (100 d)$^{-1}$. This decline slope is consistent with that expected from the decay rate of ^{56}Co into ^{56}Fe. The second decline ends at phase ∼90 d. This short fraction of the light curve will be used to guess an upper limit on the ^{56}Ni mass ejected by SN 2013gc (see Section 8). However, we will note in Section 7 that the CSM–ejecta interaction features are present in all phases of the SN evolution.

Later on, the light curve shows a sort of plateau at around 20.5, 19.0, and 18.5 mag in the *V*, *R*, and *I* bands, respectively. The plateau lasts about 70 d. We believe that the abrupt stop of the luminosity decline at +120 d marks the onset of a new, stronger ejecta–CSM interaction episode, which hereafter will become the primary source of energy for the SN. Later on, a rebrightening in the *R* and *I* bands is observed, with a rise of 1 mag. A secondary peak in the *I* band is reached on MJD 56738 (+194 d). Then, the light curve fades rapidly.

From +300 to +630 d, the light curve presents a well-defined linear decay, with a slope of 0.43 ± 0.05 mag (100 d)$^{-1}$, flatter than the decay rate of ^{56}Co. However, the SN is detected only in the *R* band. Around 2 yr after the explosion, due to the faintness of the object, the photometric measurements are very close to the detection limits.

The SN field was imaged again by the DECam Plane Survey (DECaPS, PI Rau), with the 4-m 'V. Blanco' telescope at CTIO, between January and April 2017. From this survey, we collect three stacked images in the Sloan *grz* bands. The images are calibrated using the PANSTARRS DR1 catalogue. We detect a faint source at

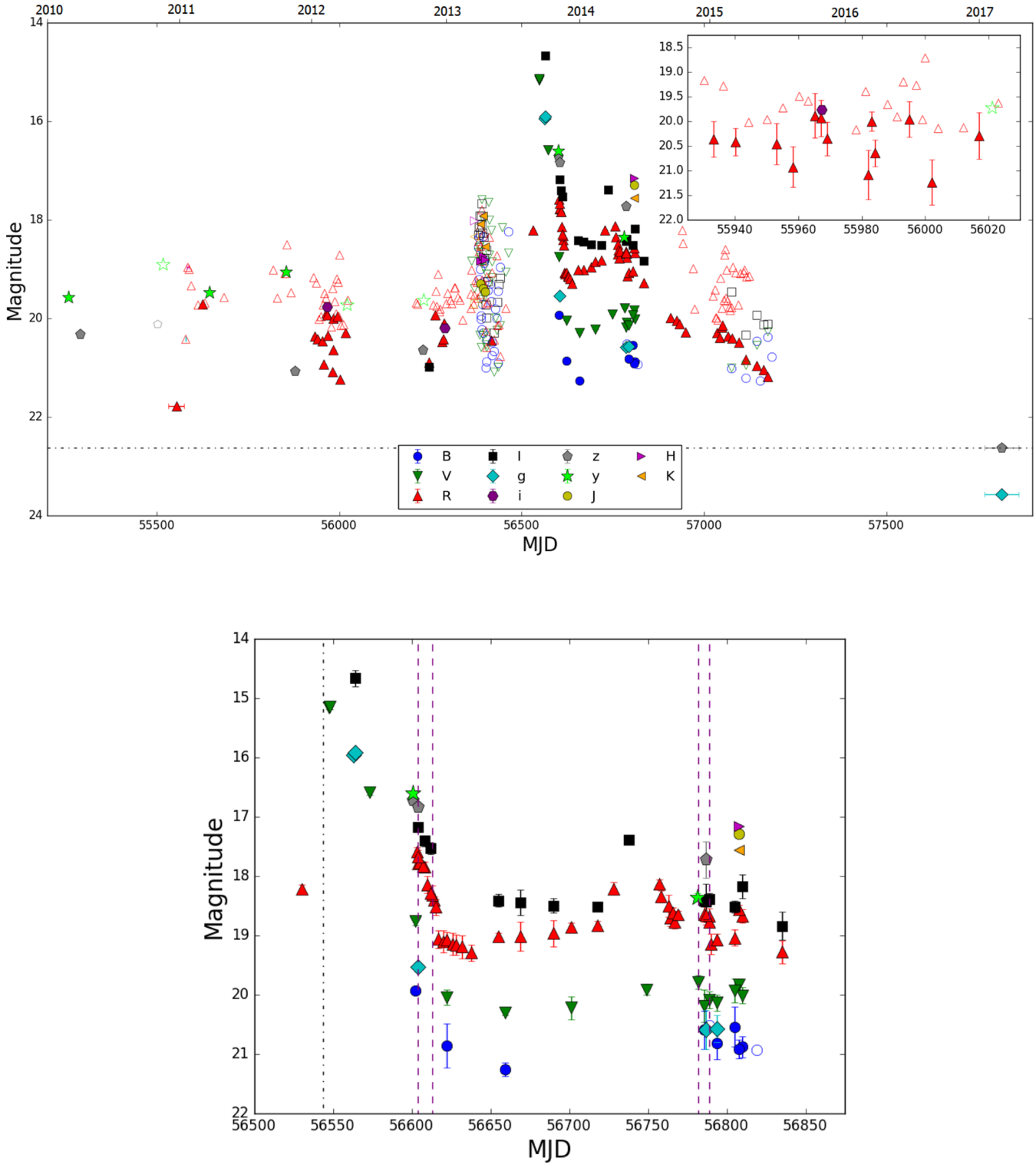

Figure 2. Optical and NIR light curves of SN 2013gc. Top: the full 7-yr coverage. For the sake of clearness, error bars are not reported here. A blow-up of the light curve of the transient during the 2012 variability period (see Section 6) is shown in the top-right inset. The horizontal line indicates the magnitude of the brightest detection of 2017, showing that the object has faded with respect to the pre-SN eruptive phase. Bottom: blow-up of the post-explosion evolution. The purple dashed lines mark the epochs of the available spectra, while the black dot–dashed line marks the date of the assumed maximum. Upper limits are indicated as empty symbols. For each band, a different symbol is used.

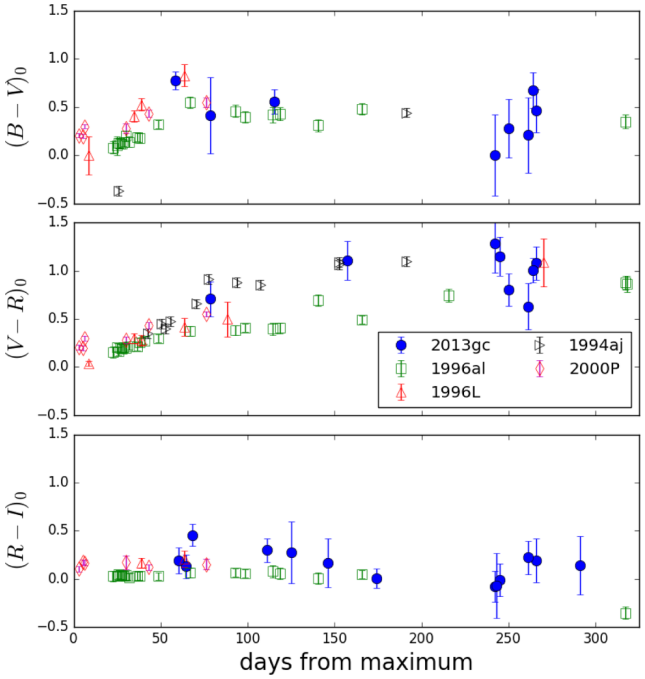

Figure 3. Colour curves of SN 2013gc (blue circles), corrected for extinction, shown with those of the comparison SNe 1996al (green squares), 1996L (red triangles), 1994aj (black triangles), and 2000P (purple diamonds). The phase of SN 2000P is from the discovery date, not from the maximum, that probably was not observed (Fig. A1). $(B-V)_0$ is in the upper panel, $(V-R)_0$ in the middle panel, and $(R-I)_0$ in the bottom panel. Error bars are reported for all objects.

the position of SN 2013gc at $g = 23.57 \pm 0.22$ mag, $r = 22.63 \pm 0.18$ mag, and $z = 22.62 \pm 0.24$ mag. These detections are over 1 mag fainter than those of the outbursts observed in 2010 to 2013, and this can be used as an argument to support the terminal explosion of the progenitor star.

5 COLOUR AND ABSOLUTE LIGHT CURVES: COMPARISON WITH SIMILAR OBJECTS

5.1 Colour curves

We compare the $(B-V)_0$, $(V-R)_0$, and $(R-I)_0$ colour curves of SN 2013gc with those of Type IId SN 1994aj (Benetti et al. 1998), SN 1996L (Benetti et al. 1999), SN 1996al (Benetti et al. 2016), and SN 2000P in Fig. 3. The photometry of SN 2000P is published in this paper for the first time, and is reported in Appendix A. For SN 1996al, we used the reddening and the distance reported in Benetti et al. (2016) [$\mu = 31.80 \pm 0.2$ mag, $E(B-V) = 0.11 \pm 0.05$ mag], while for SN 1994aj, SN 1996L, and SN 2000P we adopted the reddening and the luminosity distances reported in NED for the respective host galaxies (SN 1994aj: $\mu = 35.72$ mag, $A_V = 0.115$ mag; SN 1996L: $\mu = 35.76$ mag, $A_V = 0.255$ mag; SN 2000P: $\mu = 32.75$ mag, $A_V = 0.209$ mag). All values were obtained with the assumption $H_0 = 73$ km s^{-1} Mpc^{-1}.

Soon after maximum, the objects have colour indices around 0 mag. At early phases the $(B-V)_0$ and $(V-R)_0$ colour curves of our SN IId sample show an evolution to redder colours faster up to about 60 d, then slower until 150 d, from ∼0 to ∼1 mag. $(R-I)_0$ for SN 1996al, SN 1996L, SN 2000P, and SN 2013gc remains almost flat. At late phases (>240 d), $(B-V)_0$ increases rapidly (30 d) from

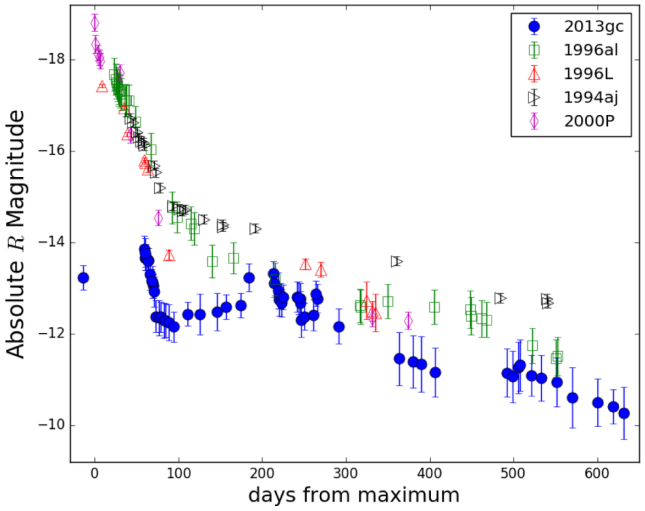

Figure 4. Absolute R-band light curves of SN 2013gc (blue circles) and comparison objects. Error bars are reported. The different symbols indicate the same SNe as in Fig. 5.

0 to 0.7 mag in SN 2013gc, as expected from a cooling photosphere (see Fig. 3). Meanwhile, $(V-R)_0$ does not have a monotonic trend, showing significant oscillations of 0.3 mag at later phases, whilst $(R-I)_0$ has a flatter evolution, stabilizing around 0 mag.

5.2 Absolute light curves

With the distance adopted in Section 2 and the extinction reported in Table 1 for SN 2013gc, we obtain $M_I \sim -16.5 \pm 0.25$ mag for the brightest observation (without accounting for the error in the reddening and in the host galaxy extinction). This value is close to the mean luminosity of 'normal' SNe IIL $\langle M_B \rangle = -16.8 \pm 0.5$ (Valenti et al. 2016) but, as discussed before, our brightest detection is not coincident with the real maximum.

The R-band absolute light curves of SN 2013gc and the Type IId SNe 1996al, 1996L, 1994aj, and 2000P are compared in Fig. 4. From this comparison, we note that the whole absolute light curve of SN 2013gc is fainter than those of comparison SNe by about 2 mag. However, the decline (between 40 and 70 d after maximum) of SN 2013gc is quite similar to the average of the sample.

Because of the low Galactic latitude of the host galaxy, the Milky Way extinction is uncertain. Shifting SN 2013gc upwards by 2 mag, a fair agreement between SN 2013gc and other SNe IId would be found, with the exception of the late rebrightening of 1 mag (lasting 40 d), which remains a distinctive feature of SN 2013gc.

The source detected in the DECam images in 2017, with $M_r \approx -8.9$ mag and an intrinsic colour $(g-r)_0 \approx 0.5$ mag, can be a contaminant background H II region or even a residual signature of the SN.

6 ANALYSIS OF PRE-SN DATA

The SN field was sparsely monitored for more than 3 yr before the explosion. We found several archival images taken between 2010 and early 2013 with a detection of a source at the SN position, although in some cases with large error bars. This is very likely an indication that the SN 2013gc progenitor experienced a long-lasting luminosity variability; most likely a major eruption started a few years before the SN explosion.

The PS1 survey sparsely monitored the field between 2010 and 2013. The first PS1 images of March 2010, in the z and y bands, show a source with a magnitude of about 20. Then, a stack of the nine best-quality frames taken between 2010 December 2 and 2011 January 14 from the PTF survey (PI Rau) has been produced. In this deep image, we detect a very faint source at $R \sim$21.8 mag, which is close the bona-fide limiting magnitude of the survey. The absolute magnitude of the source is only $M_R \sim -9.65$ mag. From the same survey, we combine the images obtained from 2011 January 17 to 19 and from 2011 January 21 to 27. The seeing of those nights was quite poor (3 arcsec), and only upper limits are obtained.

We found a few images taken later in 2011, with only one detection on 2011 March 06 (MJD 55626). For this event we estimate $M_R = -11.74 \pm 0.35$ mag, although we cannot constrain the duration of the outburst. In fact, in frames obtained 12 d before and 6 d after the burst, nothing is visible at the same limiting magnitude.

In early 2012, the field was well monitored, and a few additional sparse detections are found (see the top-right box in Fig. 2). This provides additional evidence of the long-lasting photometric instability of the SN progenitor. The faintest detections are at 21 mag, corresponding to $M_R \sim -10.5$ mag, but in other cases the source has an apparent mag between 20 and 21. The source has also been detected by PS1 on 2011 October 20 in the y band, at 19 mag, which is almost 3 mag brighter than the faintest PTF detection measured 9–10 months before. We now describe a sequence of events: on 2012 February 25 (MJD 55982), the source is hardly visible. The day after, the object is in flare, showing a brightening of 1 mag. Then, on 2012 February 27, the transient has faded again by 0.5 mag (inset of Fig. 2). This sequence highlights a scenario with short-duration flares occurring during a long eruptive phase. The absolute magnitude estimated for this flare is $R = -11.41 \pm 0.40$ mag, similar to that observed in sole LBV-like outburst, such as SN 2000ch (Wagner et al. 2004). The upper limits measured in a number of lower-quality images are not very deep (<20 mag); hence, they are not very constraining.

After some months without images due to the heliac conjunction, the monitoring campaign restarted in late 2012, and the object was detected in several frames. In one of them, on 2012 December 1, the object reached $M_R = -11.51 \pm 0.50$ mag. In March 2013, the explosion of SN 2013ak in the same galaxy triggered a vast observational campaign, and tens of multiband images of the field are hence available. In one of those images, taken with the Gemini-South telescope, a brightening is clearly revealed on 2013 May 4 at $R = 20.45$ mag ($M_R \sim -11.00 \pm 0.23$ mag). Also this event is probably a short-duration flare. In fact, the source is not detected in images taken one day before and one day after. However, the quality of these images, taken with the PROMPT telescopes, is lower than the image of the Gemini South telescope. We remark that the peak luminosity of the four impostor events described above is very similar. After June 2013, the region was again in heliac conjunction. Then, when the field again became visible at around mid-August 2013, the SN was already visible.

7 SPECTROSCOPY

We obtained five optical spectra of SN 2013gc with the following two instrumental configurations:

(i) The 4.1-m 'SOAR' telescope at CTIO, with the Goodman Spectrograph[12] (PI F. Bufano).

(ii) The Du Pont telescope at Las Campanas Observatory with the WFCCD/WF4K[13] (PI P. Lira).

The pointing images of these instruments were also used for photometry. The first spectrum, taken one day after the discovery, was used for the spectral classification. The second spectrum is dated 2013 November 17, during the first dimming phase. The last two spectra were obtained after the second luminosity peak, on 2014 May 5 and May 12. On 2014 May 12 a medium-resolution spectrum around the Hα region was also taken. Technical details of the five spectra are reported in Table 2.

7.1 Spectroscopic reduction and line identification

All spectra were pre-reduced and calibrated using routine IRAF packages. The two-dimensional frames were corrected for bias and flat-field, and then the one-dimensional spectra were extracted and sky lines and cosmic rays were removed. On that spectrum, we performed wavelength and flux calibrations, using arc lamps and spectrophotometric standard stars. The spectral fluxes were scaled according to the R-band photometry of the nearest night. The spectra were also corrected for the strongest telluric absorption bands. The five spectra were corrected for redshift and reddening, adopting the values of z and A_V given in Table 1. The calibrated low-resolution spectra, with line identification, are shown in Fig. 5, while the medium-resolution spectrum is plotted in the bottom panel.

A weak red continuum ($T_{\rm bb} \sim 4000$ K) is present in the early spectra. Absorption features of metals and Balmer lines in emission are also observed. Hα is the most prominent feature in all the spectra, and its profile is described in detail in Section 7.3. Hβ has a profile similar to that of Hα. Hγ is not clearly detected, although the spectra have a low SNR at the blue wavelengths. He lines are weak in the early spectra, but become more intense later. He I λ7065 is the stongest line, followed by λ6678 and λ4922. He I 5876 is blended with the Na ID doublet in emission.

To evaluate the evolution of the He lines, we measure the flux ratio Hα/He I λ7065 in all the spectra. We choose the He I λ7065 line because it is isolated and not significantly blended with other lines. In the first two spectra, the ratio is around 90 ± 10, but the flux measurement of the He line is difficult due to its faintness. In the +238 d spectrum, the ratio is lowered to ~30, and in the +245 d spectra it is only 18 ± 2.

We identify Fe II features (multiplets 40, 42, 46, 48, 49, 199). The Fe II (46) λ6113 line is observed in absorption at early phases, while it is in emission at late epochs.

At late phases, the flux contribution of the spectral continuum is negligible, and the line profiles have changed. We identify the Ca II IR triplet lines, detected as broad emission. The FWHM of the Ca II λ 8662 line is 3400 ± 100 km s^{-1}. There is a possible detection of O I λ7774 in the first spectrum. More in general, we note an increasing

[12]It has a 7.2-arcmin-diameter FOV, with a 0.15 arcsec per pixel scale. We used the Red Camera. The Spectrograph can also do imaging. The Red Camera is equipped with a 4096 × 4112 pixel, back-illuminated, E2V CCD (http://www.ctio.noao.edu/soar/content/goodman-red-camera).

[13]The camera covers a 25 arcmin field, with a scale of 0.484 arcmin per pixel. The detector has 4064 × 4064 pixels (http://www.lco.cl/telescopes-information/irenee-du-pont/instruments/).

Table 2. Basic information of the five spectra of SN 2013gc. The phase is with respect to the adopted maximum (MJD 56544). To evaluate the instrumental resolution, we measured the FWHM of the [O I] night sky lines.

Date	MJD	Phase (d)	Instrument	Sky lines FWHM (Å)	Spectral range (Å)	Exp. times (s)
2013 Nov 8	56604.20	+60	WFCCD + blue grism	8.2	3620-9180	2 × 900
2013 Nov 17	56613.17	+69	Goodman Spectrograph	5.0	3765-8830	2 × 3600
2014 May 5	56782.09	+238	WFCCD + blue grism	7.7	3630-9200	2 × 1000
2014 May 11	56788.98	+245	Goodman Spectrograph	7.6	4050-8940	2 × 2700
2014 May 12	56789.05	+245	Goodman Spectrograph	1.7	6250-7500	2700

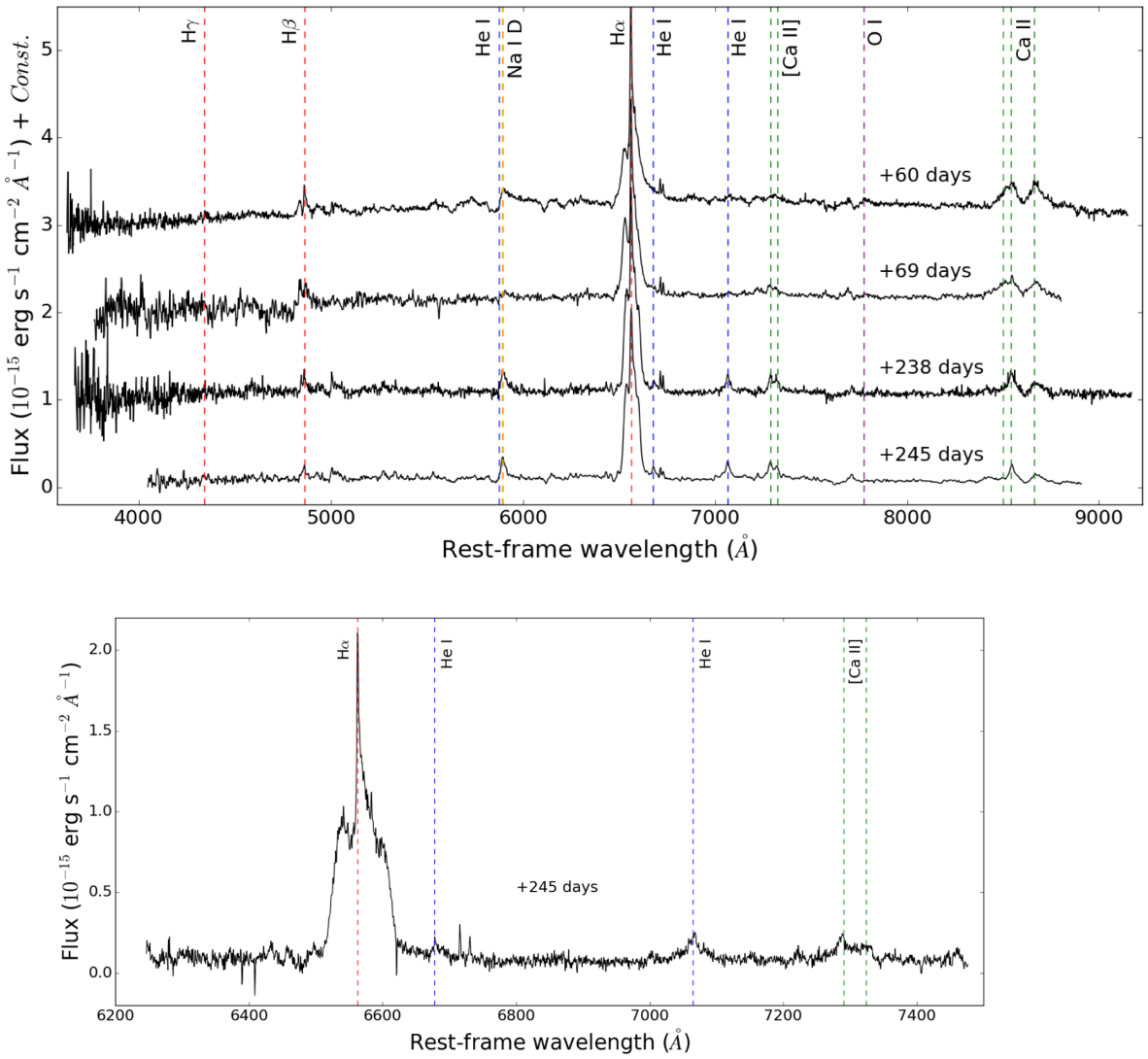

Figure 5. Top: the four low-resolution spectra of SN 2013gc, corrected for redshift and reddening. Bottom: the mid-resolution spectrum of SN 2013gc, dated 2014 May 12. The spectrum covers 1200 Å around the H α line. The most prominent lines are identified in the figure.

number of emission lines, especially from forbidden transitions. In particular, we identify [N II] λλ 6548, 6584 lines (although blended with the H α line); [S II] λλ 6716, 6731 lines; and [Ca II] λλ 7291, 7324 lines. Narrow [O III] λλ 4959, 5007 lines are superimposed on broader Fe II feature emission. Narrow [S II], [N II], and [O III] lines likely arise from unresolved background contamination. In fact, in a 2012 image taken by the VST telescope equipped with OMEGACAM and a narrow H α filter during the VPHAS + survey (PI Drew), a diffuse, elongated source is visible. This object can be a foreground H II region. In contrast with other forbidden lines, [Ca II] lines are attributed to the SN environment, and seem to become stronger with time.

7.2 Comparison with similar objects

Our spectra are compared with those of SN 1996al, SN 1996L, SN 1994aj, and SN 2000P obtained at around the same phases. All spectra of SN 2000P are presented in this paper for the first time (see Appendix A).

The early spectra of SN 2013gc are similar to those of SN 1994aj, SN 1996al, and SN 1996L taken at 60–70 d after maximum, in particular with respect to the H α profile and the Na ID P-Cygni line. In all these SNe, H α and H β show a narrow P-Cygni absorption over a broader P-Cygni component. The main difference at early times is that SN 1996L has a hotter continuum, peaking around 5000 Å, giving a blackbody temperature T_{bb} of ∼6000 K.

One of the most interesting comparisons is with SN 2000P, which has an excellent spectroscopic data set. As for SN 2013gc, H α is characterized by a very narrow P-Cygni absorption and an extended Lorentzian red wing. H β has a similar narrow P-Cygni feature. Many bumps, likely due to Fe II, are observed in the spectra of both objects. It is worth comparing the spectra and the H α profile evolution of SN 2000P (Fig. A2) with those of SN 1996al (figs 5 and 7 of Benetti et al. 2016). In the spectra of SN 2000P obtained a very few days after the maximum light, the blue continuum indicates a high gas temperature. H α and H β show a double P-Cygni feature, along with a broad emission from He I λ5876 and Na ID lines. At phase +30 d, many bumps from metals arise and the Ca II triplet becomes well visible; similar features are visible in the first spectrum of SN 2013gc. From this epoch, a blueshifted H α bump starts to develop at an intermediate width, and grows in strength with time. One year after the maximum, H α is nearly the only observable feature, and the blueshifted component is more prominent than that at the rest frame.

The late-time spectra of SN 2013gc and SN 2000P are not sufficiently close in phase to make a reasonable comparison. A comparison of the spectra of SN 2013gc with those of other SNe IId at similar phases is provided in Fig. 6. In the comparison of early-time spectra, we note that H β is quite prominent, with the Balmer decrement H α/H β being higher in SN 2013gc than in other SNe IId. In particular, for SN 1996al at ∼ +60 d, Benetti et al. (2016) found an H α/H β ratio of 5, while in SN 2013gc we infer a ratio of around 10. In the late spectra the ratio increases to ∼20. This comparison with SN 1996al supports the possibility that the reddening in the direction of ESO 430-20 may have been underestimated.

7.3 The H α profile

The analysis of the H α profile can provide information on the CSM around the SN. The H α profile is complex, and consists of multiple components (see Fig. 7). In the early spectra, a narrow P-Cygni absorption is superposed on a broad component. The line is asymmetric, with an extended red wing. The simultaneous presence of a broad component from the fast ejecta and a narrow P-Cygni profile from slow circumstellar wind is a characterizing feature of Type IId SN spectra. The H α profile shows an evolution from the early (+60 d) to the late (+245 d) epochs, with the velocities of the broader components progressively decreasing with time. In order to identify the different line components, we deblended the H α profile, following Benetti et al. (2016). We considered the spectra obtained +69 and +245 d. The results are illustrated in Fig. 8, and the velocities of the different line components are reported in Table 3.

In the early epoch, the relatively broad H α component has a velocity of 3400 km s^{-1}, which is very similar to the FWHM velocity (v_{FWHM}) of the Ca II λ8662 line. The FWHM of this component can be considered representative of the SN ejecta velocity. In the late spectrum, H α has been deblended using three distinct intermediate-width emission components, with comparable v_{FWHM} ranging between 1300 and 1800 km s^{-1}. These components correspond to three distinct emitting regions: a first one (blueshifted from the rest wavelength) moving towards the observer, a second (redshifted) one produced by receding gas, and a third one, centred at the rest frame.

In principle, from the velocities of the ejecta and the CSM, one can infer the time of ejection of the CSM which later interacts with the SN ejecta. We adopt the velocities derived from the first spectrum, because it is the closest available to the explosion. We adopt 3400 km s^{-1} for the ejecta (from the FWHM of the broad component), and 560 km s^{-1} for the wind (from the minimum of the narrow P-Cygni component). Although the velocity at the explosion should be used for freely expanding ejecta, those of SN 2013gc are likely shocked already soon after the explosion; hence, the value inferred from the first spectrum is a fair approximation of the ejecta velocity. The explosion epoch is unknown, but it is constrained between MJD 56463 (the last non-detection) and MJD 56530 (the first SN detection). Assuming that the collision of the SN ejecta with a dense circumstellar shell marks the onset of the light-curve plateau (MJD 56640 ± 10), the material would have been ejected between MJD ∼55560 (December 2010–January 2011) and MJD ∼55970 (February 2012) for the above two constraints on the explosion epoch, respectively. On the other hand, at about MJD 56720 ± 10, we note a major brightening of the light curve, which is an evidence of enhanced CSM–ejecta interaction. With the same velocities and the explosion time interval, the second shell would have been ejected between MJD ∼55150 (November 2009) and MJD ∼55560 (December 2010–January 2011). The above constraints on the mass-loss epochs are consistent with the timing of the pre-SN detections, and favour an explosion occurring soon after the last non-detection (Section 6 and Fig. 2, top panel). From March 2010, we directly witnessed the outbursts that produced the SN CSM and determined the Type IIn/IId observables.

8 DISCUSSION

The composite Balmer line profiles, with the simultaneous presence of broad and narrow components with P-Cygni profiles, make SN 2013gc a member of the IId subclass of Type IIn SNe (Benetti 2000). This fact is supported by the comparison of the colour and absolute light curves of SN 2013gc with those of known SNe IId, which show a similar evolution. In particular, the onset of strong ejecta–CSM interaction in SN 2013gc (between 120 and 140 d after the explosion) is compatible with that observed in similar SNe (typically between 100 and 150 d; Benetti 2000).

8.1 Bolometric luminosity and ^{56}Ni mass

We calculated the pseudo-bolometric light curve of SN 2013gc accounting for the contribution in the *BVRI* bands only. For epochs without observations in some bands, we made an interpolation to the available data using the *R*-band light curve as reference, and assuming a constant colour index. The maximum is not covered by *R*-band images; hence, to constrain the peak luminosity, we calculated the pseudo-bolometric light curve accounting only for the *gVIz* band contribution. We assumed the $V-I$ and $V-z$ colours to be constant between 30 and 80 d after the explosion, at 1.5 and 2.0 mag, respectively, as derived from the closest photometry of 2013

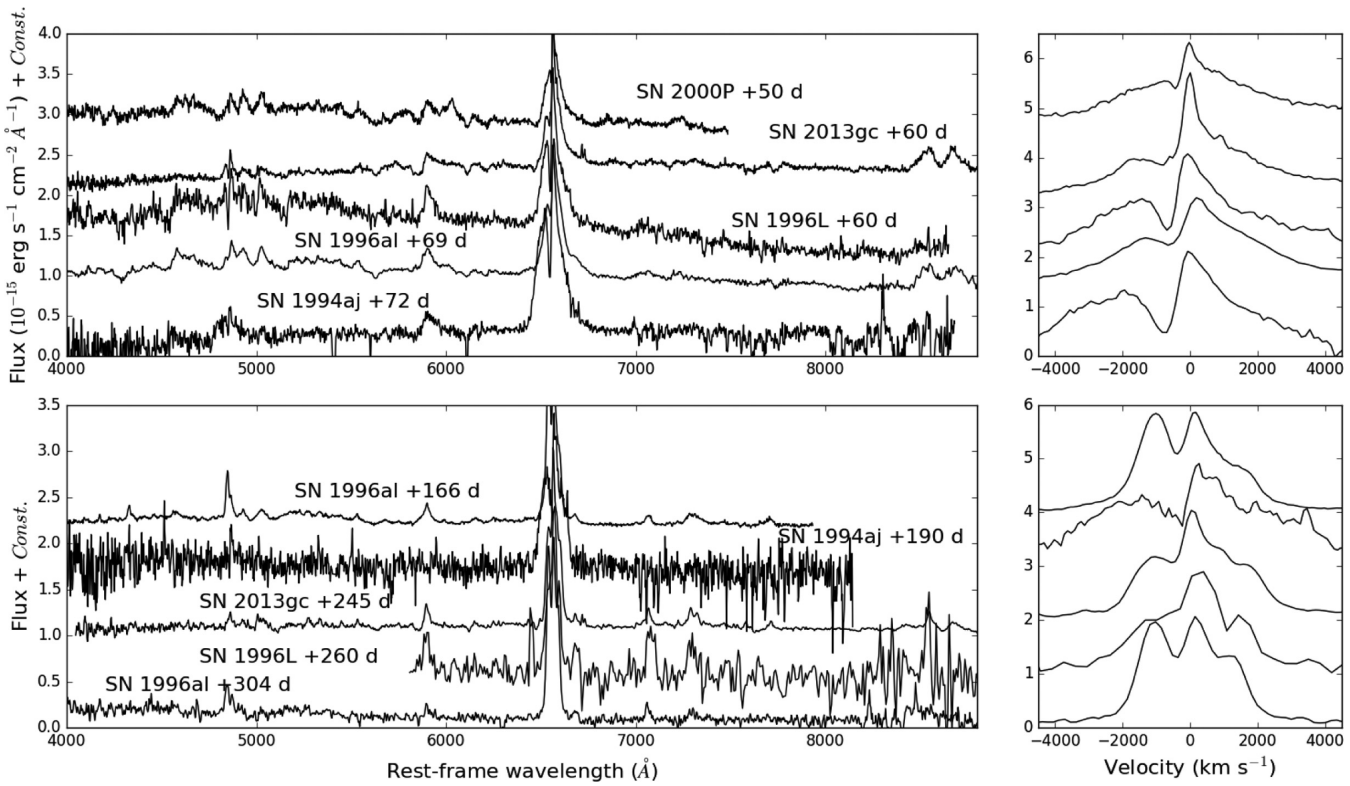

Figure 6. Comparison of the +60 (top) and +245 (bottom) d spectra of SN 2013gc with those of reference SNe IId at approximately the same phase. In the right-hand panel, the same comparison is done for Hα profiles at the same epochs.

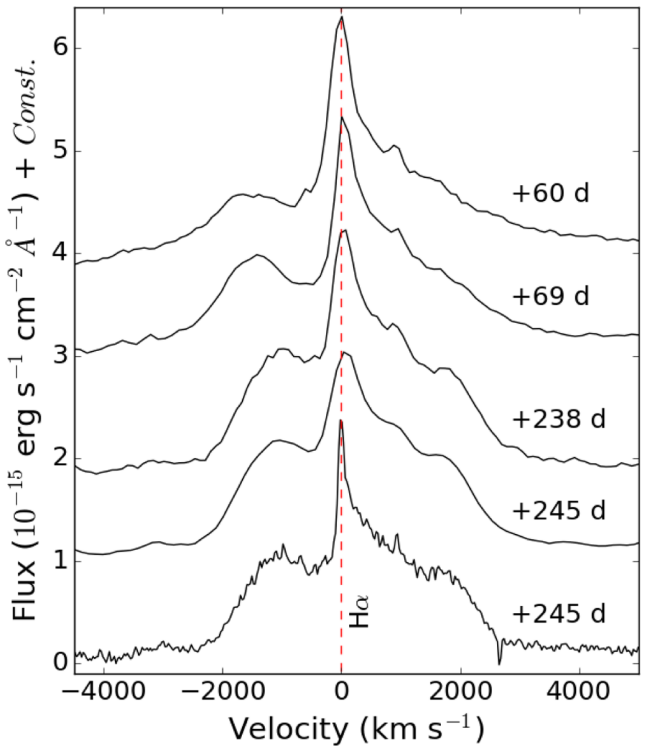

Figure 7. Blow up of Hα line in the five available spectra. Velocities with respect to the rest frame are reported in abscissa. The zero velocity is marked with a dotted line.

November 7. We fixed the explosion date on MJD 56520 ± 7, about 10 d before the first SN detection. This implies a rise time of 23 ± 7 d from the explosion to the maximum. Then a first steep decline is observed. In order to estimate an upper limit of the ejected ^{56}Ni mass, we focus on the light-curve portion having a decline slope similar to that of ^{56}Co. We identify a very short time interval during which the decline slope is compatible with the ^{56}Co decay rate, that is between 97 and 118 d after explosion.

As a comparison, we selected the classical core-collapse SN 1987A and a Type II SN with a shorter plateau, SN 2012A (Tomasella et al. 2013). The choice of SN 2012A was motivated by the fact that the putative ^{56}Co decay tail started early in SN 2013gc, at ∼100 d, when typical Type IIp SNe are still in the plateau phase, or during the steep post-plateau luminosity decline. In contrast, SN 2012A was a short-duration IIp event, whose light curve was already following the ^{56}Co decay at 100 d. Hence, this is a more reliable comparison object to estimate the ^{56}Ni mass of SN 2013gc. SN 1996al is also considered as a comparison object. The bolometric light curves of the four objects are compared in Fig. 9, with a blow-up of the portion of the SN 2013gc light curve with a decline rate consistent with the ^{56}Co decay.

The estimated ^{56}Ni mass of SN 1987A is 0.085 $M_\odot$ (Utrobin & Chugai 2011), while for SN 2012A the estimate is 0.011 ± 0.004 $M_\odot$ (Tomasella et al. 2013). We calculated and averaged the bolometric luminosity ratio of SN 2012A and SN 2013gc at three epochs after the explosion, at +112, +118, and +135 d. These three epochs were selected because at the same phases SN 2012A was declining with a rate consistent with the ^{56}Co decay. The $M_{\rm Ni}^{56}$ is obtained from

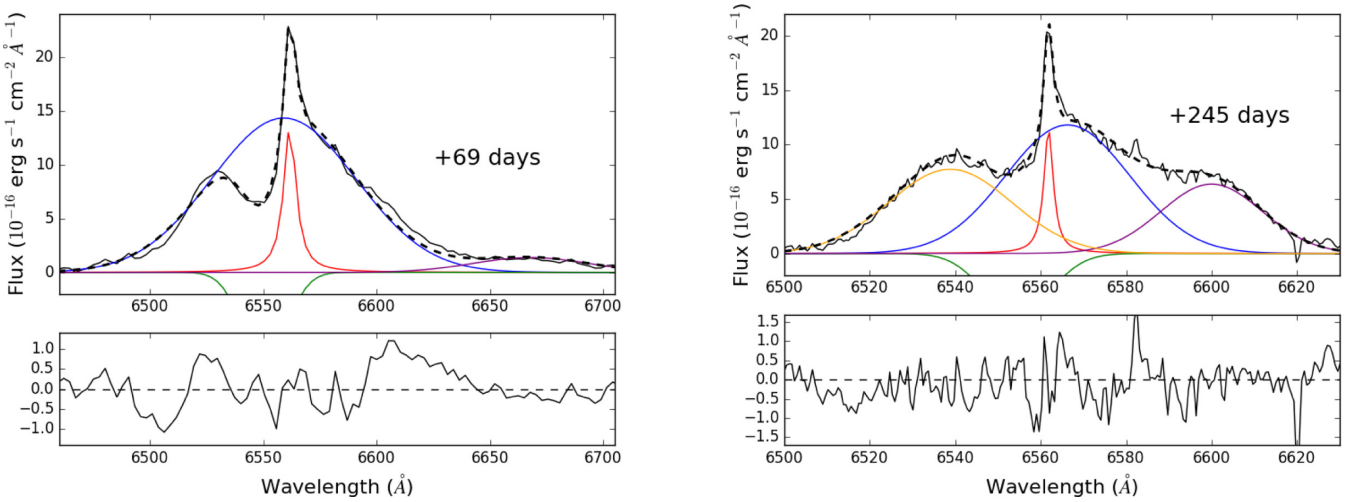

Figure 8. Decomposition of the H α profile through multiple components. Left: In the +69-d spectrum the profile is well fitted using a broad Gaussian emission (blue), on top of which a narrow Lorentzian emission (red) stands, and a Gaussian absorption (green) for the P-Cygni. The bump due to the He I λ6678 is also fitted with a Gaussian emission (purple). Right: In the mid-resolution (FWHM = 1.7 Å) +245-d spectrum, the H α profile is decomposed with an intermediate-width Gaussian emission (blue), a narrow Lorentzian emission (red), and a Gaussian absorption for the P-Cygni (green). Two additional Gaussian components are required, redshifted (purple) and blueshifted (orange). In both graphs, the sum of the four components is shown with a black dashed line. Residuals between the data and the fit are reported in the bottom panels.

Table 3. FWHM and central wavelengths of the various components of the H α profile in all spectra. For the P-Cygni component, the velocity of the minimum with respect to the rest frame is reported.

Phase	$(Em)_{broad}$	$(Em)_{narrow}$	$(Ab)_{P\text{-}Cygni}$	Red wing	Blue wing
(d)	v_{FWHM}; λ_c (km s^{-1});(Å)	v_{FWHM}; λ_c (km s^{-1});(Å)	Min. vel. (km s^{-1})	v_{FWHM}; λ_c (km s^{-1});(Å)	v_{FWHM}; λ_c (km s^{-1});(Å)
+60	3400 ± 100; 6559	300 ± 15; 6561.7	560		
+69	3450 ± 100; 6557	340 ± 20; 6561.7	470		
+238	1600 ± 50; 6565	420 ± 20; 6561.2	420	1800 ± 50; 6598	1600 ± 50; 6540
+245	1600 ± 50; 6566	350 ± 20; 6563.5	460	1650 ± 50; 6598	1600 ± 50; 6542
+245	1550 ± 50; 6566	120 ± 5; 6561.8	380	1300 ± 30; 6600	1550 ± 50; 6539

the following relation:

$$\frac{L_{bol}(2012A)}{L_{bol}(2013gc)} = \frac{M_{Ni}^{56}(2012A)}{M_{Ni}^{56}(2013gc)} = 2.6^{+3.8}_{-1.1} \quad (1)$$

The error bars account also for the uncertainty in the explosion epoch. From this value, and propagating the errors, the ^{56}Ni mass estimated for SN 2013gc is $4.2(^{+5.8}_{-3.2}) \times 10^{-3}$ M$_\odot$. We remark that this value has large uncertainties, because at 135 d the ejecta–CSM interaction becomes very strong, and the light curve becomes flatter than the ^{56}Co decay. For this reason, the above value of the ^{56}Ni mass should be regarded as an upper limit. On the other hand, we cannot rule out that an optically thick shell is hiding interior emission, leading us to underestimate the ^{56}Ni mass. It is worth noting that for SN 1996al Benetti et al. (2016) constrained an upper ^{56}Ni mass limit of 0.018 M$_\odot$, a factor of about 4 higher than that inferred for SN 2013gc.

This ^{56}Ni mass constrained for SN 2013gc is definitely modest, also accounting that other photometric indicators (in particular, the plateau and the second brightening) suggest that the main luminosity-powering mechanism is the interaction between the SN ejecta and the surrounding material. For this reason, the ^{56}Ni mass ejected by SN 2013gc is most likely very low, comparable with that inferred for some underluminous Type II SNe (Pastorello et al. 2004; Spiro et al. 2014).

8.2 The progenitor star

The interest for SN 2013gc lies in the fact that a prolonged variability phase was observed at the progenitor site before the SN explosion. So far, only one possible eruptive event was claimed for the progenitor of a SN IId. It was a single detection of a luminous source at the position of SN 1996al in archival H α images obtained 8 yr before the SN explosion (Benetti et al. 2016). For SN 2013gc the indications of pre-SN stellar activity are much more robust, as we witnessed a complex long-lasting eruptive phase prior to the explosion. As seen in Section 6, the variability of the progenitor in 2010–2012 resembles those observed in other SN impostors, in particular the pre-SN stages of SN 2009ip (Mauerhan et al. 2013; Pastorello et al. 2013) and SNhunt 151 (Thöne et al. 2017; Elias-Rosa et al. 2018) and the current evolution of SN 2000ch (Pastorello et al. 2010). The bright absolute magnitude of the source in pre-SN images ($M \sim -11$ mag) rules out the possibility that the progenitor was in a quiescent phase.

The deconvolution of the H α profile, in particular from the last spectrum, allows us to reconstruct the structure of the CSM and to constrain the physics of the explosion and the nature of the progenitor star.

The fast initial (50–80 d) drop of the light curve implies small ejected H mass. Modest ejected mass is consistent with two SN scenarios: the low-energy explosion of a relatively low-mass progen-

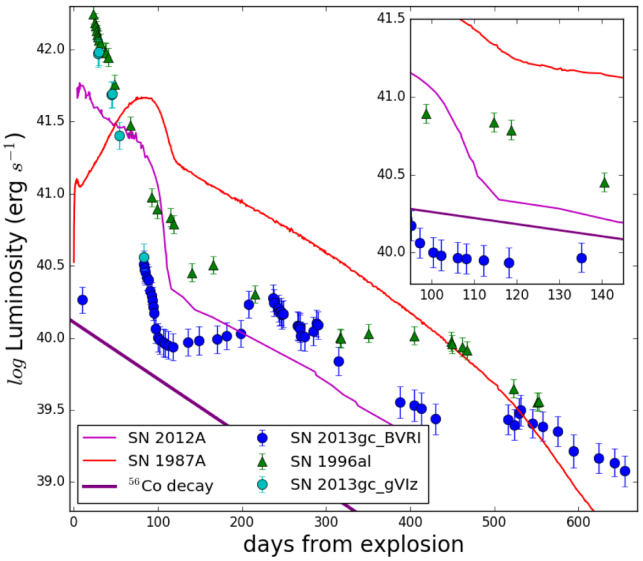

Figure 9. Quasi-bolometric *BVRI* light curves of SNe 1987A, 1996al, 2012A, and 2013gc. The inset shows a blow-up of the region between 95 and 145 d after the explosion, in which there is evidence of ^{56}Co radioactive decay. The decay slope of ^{56}Co [0.98 mag (100 d)$^{-1}$] is reported with a purple line for comparison. The early-phase (*gVIz*) bolometric light curve is plotted with cyan dots.

itor (7–8 $M_{\odot}$) or, alternatively, a very massive progenitor (M_{ZAMS} > 25 $M_{\odot}$) ending its existence as a fall-back SN. Assuming a low-mass-progenitor scenario, the pre-SN eruptive phase can be attributed to binary interaction or, alternatively, to a super asymptotic giant branch phase during which a star loses mass generating a circumstellar cocoon, before exploding as an electron-capture SN (e.g. Nomoto 1984; Kitaura, Janka & Hillebrandt 2006; Pumo et al. 2009). In the massive-progenitor scenario, the star core collapses into a black hole, as most of the stellar mantle falls back on to it. In this way, only the most external layers are ejected. A fall-back SN is also consistent with the low ejected ^{56}Ni mass (Zampieri et al. 1998; Moriya et al. 2010), because the inner regions of the star rich in heavy elements remain bound to the collapsed core. A fall-back SN produces a faint explosion. The absence of [O I] λλ 6300, 6364 lines in the late spectra is also in agreement with the expectations of the fall-back SN scenario (Valenti et al. 2009), but can alternatively be explained as due to an optically thick region of interaction, which hides the O-rich ejecta.

High-mass stars, such as LBVs and Wolf–Rayet stars, are known to experience severe mass loss via superwinds during the final stages of their life. When they finally produce a core-collapse SN, the material ejected by the SN will interact with the composite circumstellar environment. LBVs are suitable progenitor candidates for types IIn/IId SNe. Such LBV candidates would pass through an eruptive phase with many alleged outbursts that create a complex and structured CSM. The interaction of the SN ejecta with this CSM would produce unusual features in the light curve, like the plateau and the observed rebrightening.

A third, somewhat different scenario is a non-terminal explosion event. The precursor activity exhibited by SN 2013gc shares some similarities with the pre-explosion variability of SN 2009ip. The nature of this object and its fate after the two 2012 events are still somewhat disputed, and a non-terminal mechanism has also been proposed (Pastorello et al. 2013; Margutti et al. 2014). This scenario would be consistent with many characteristics of SN 2013gc, including no ^{56}Ni production, the lack of [O I] lines, and the faint absolute magnitude. In this context, the source detected in the 2017 DECAPS images might be the survived progenitor. As a consequence, the brightest event would have been an SN impostor that generated a fast-moving shell. The following photometric evolution would result from the shell–shell collision. We note, however, that the putative progenitor recovered in the DECAPS images was much fainter than the hystorical detections, still favouring the SN explosion for the 2013 event.

We propose two physical mechanisms that possibly drove the precursor variability. Pulsational mass loss in very massive stars, possibly triggered by a pulsational-pair Instability, can be accompanied by large luminosity variations (Woosley, Blinnikov & Heger 2007). As an alternative, mass loss can be triggered by stellar interaction in an LBV binary system, with eccentric orbits. When the secondary approaches the periastron, the tidal forces can strip away part of the material of the primary, enhancing the mass loss and the luminosity (Pastorello et al. 2010). If this is the case, a modulation can be observed in the light curve. The observations do not firmly support one of the two scenarios, because of the modest signal to noise of the available photometry and the lack of adequate cadence.

8.3 The explosion scenario

From the decomposition of the Hα profile, we can constrain the geometry of the CSM. The presence of multicomponent Hα line profiles in both early- and late-epoch spectra reveals that the CSM–ejecta interaction was likely active from the early phases of the SN evolution, suggesting that the progenitor's mass loss continued until a very short time before the SN explosion. In this context, the above claim is supported by the evidence that the progenitor in outburst was observed until May 2013, only ∼100 d before the SN explosion. The light-curve plateau and the rebrightening at about 200 d have to be considered as enhanced interaction with a denser CSM regions.

The Hα profile in the late spectra has a composite profile, with three intermediate-width components (with v_{FWHM} exceeding 10^3 km s^{-1}): a blueshifted component peaking at −1000 km s^{-1}, a redshifted one centred at +1600 km s^{-1}, and a third one in the middle, centred at the rest wavelength of the transition, atop which a narrow emission is observed with v_{FWHM} of a few 10^2 km s^{-1}. This suggests a complex and structured CSM geometry.

The two components shifted from the rest wavelength reveal a bipolar emitting structure of the CSM, expanding with a core velocity in the range 1300–1800 km s^{-1}. The difference of the measured expansion velocities can be explained with an intrinsic difference in the ejection velocity of the two lobes, or possibly by a mismatch between the line of sight and the polar axis of the bipolar nebula. Similar spectral features were observed in the SN IIn 2010jp, although in that case a jet-like explosion in a nearly spherically symmetric CSM was proposed (Smith et al. 2012), and the velocities involved were in fact one order of magnitude larger. The kinetic energy of SN 2013gc is much smaller, and is consistent with a fall-back SN scenario (see Section 8.2). A spherically symmetric CSM expanding at a much lower velocity is revealed through the presence of a narrow Hα component, while a nearly spherical shell, shocked by the interaction, produces the central, intermediate-width component. The material shocked by the ejecta is optically thick and hides (at all epochs) the underlying SN features.

This CSM configuration shares some similarity with that proposed by Benetti et al. (2016) for SN 1996al, consisting of an

equatorial circumstellar disc producing the Hα profile with two emission bumps shifted from the rest wavelength. That material was surrounded by a spherical, clumpy component producing the Hα emission at zero velocity. The clumpiness of the SN 1996al CSM was deduced from the evolution of the He lines, which became more prominent with time. In analogy with SN 1996al, the spectra of SN 2013gc show an increasing strength of the He lines from the early to the late phases, which may indicate the presence of higher-density clumps heated by the SN shock in its lower-density, spherically symmetric CSM component. We also note that the radial velocities of the Hα bumps of SN 1996al and SN 2013gc are comparable, supporting an overall similarity in the gas ejection scenarios for the two objects. SN 1996al was characterized by low ejecta mass and a modest kinetic energy. The ejecta interaction with a dense CSM embedding the progenitor determined the light-curve features at all phases, and was still active 15 yr after the explosion. The proposed CSM structure around SN 2013gc is composed of an equatorial disc with a complex density profile, and ejecta–CSM interaction being always present. When the ejecta reach the first CSM equatorial density enhancement, the conversion of kinetic energy into radiation gives rise to the observed plateau, while the encounter with an outer layer with higher density powers the second peak. Later on, ejecta–CSM interactions weaken and the SN light curve finally starts the fast decline.

9 CONCLUSIONS

SN 2013gc is a member of the Type IId SNe class, a subgroup of Type IIn SNe whose spectra are characterized by double, broad and narrow, P-Cygni Hα components. SN 2013gc can be considered a scaled-down version of SN 1996al, triggered by the same physical process: a fall-back SN from a highly massive star, possibly an LBV. SN 2013gc is the first object of this class showing a long-duration progenitor's eruptive phase lasting a few years (at least from 2010 and 2013), which continued until a very short time before the SN explosion. The object showed significant variability, with oscillations of 1–2 mag in very short time-scales (days to months). The multiple flares and the long-duration major eruption are best suited to a massive progenitor in its final evolutionary stages, very likely an LBV. The outbursts formed a structured CSM around the progenitor (and very close to it), and the SN ejecta interact with it from soon after the SN explosion. When the ejecta collide with denser CSM layers, the interaction powers the observed light-curve plateau and the second peak. The CSM is likely clumpy, as deduced from the evolution of the He lines, and is composed of a spherically symmetric component, two denser shells, and a further bipolar CSM component. The fall-back scenario of a massive star is supported by the low ^{56}Ni mass found, the low luminosity of the SN, the lack of [O I] lines in the spectra, and the detection of numerous pre-SN outbursts from the progenitor. We note, however, that the observables of SN 2013gc are not inconsistent with a non-terminal outburst, followed by shell–shell collision.

ACKNOWLEDGEMENTS

We thank the anonymous referee for helpful comments that improved our paper.

This research has made use of the NASA/IPAC Extragalactic Database (NED), which is operated by the Jet Propulsion Laboratory, California Institute of Technology, under contract with the National Aeronautics and Space Administration.

Support for G.P. and F.O.E. is provided by the Ministry of Economy, Development, and Tourism's Millennium Science Initiative through grant IC120009, awarded to The Millennium Institute of Astrophysics (MAS). F.O.E acknowledges support from the FONDECYT grant N° 11170953. The CHASE project is founded by the Millennium Institute for Astrophysics.

Based in part on data obtained from the ESO Science Archive Facility under programme IDs 188.D-3003, 177.D-3023 for SN 2013gc, 65.H-0292(D), 66.D-0683(C), 69.D-0672(A), 67.D-0422(B), 71.D-0265(A), 65.I-0319(A), 65.N-0287(A), 67.D-0438(B), 77.B-0741(A) for SN 2000P. We thank G. Altavilla for the support on the observations of SN 2000P.

Based in part on observations obtained at the Southern Astrophysical Research (SOAR) telescope, which is a joint project of the Ministério da Ciência, Tecnologia, Inovações e Comunicaçãoes (MCTIC) do Brasil, the U.S. National Optical Astronomy Observatory (NOAO), the University of North Carolina at Chapel Hill (UNC), and Michigan State University (MSU).

Based in part on observations at Cerro Tololo Inter-American Observatory, National Optical Astronomy Observatory (NOAO), which is operated by the Association of Universities for Research in Astronomy (AURA), Inc. under a cooperative agreement with the National Science Foundation. The Dark Energy Camera Plane Survey (DECaPS; NOAO Program Number 2016A-0323 and 2016B-0279, PI: Finkbeiner) includes data obtained at the Blanco telescope, Cerro Tololo Inter-American Observatory, National Optical Astronomy Observatory (NOAO).

The SARA Observatory is supported by the National Science Foundation (AST-9423922), the Research Corporation, and the State of Florida Technological Research and Development Authority.

This research has made use of the NASA/IPAC Infrared Science Archive, which is operated by the Jet Propulsion Laboratory, California Institute of Technology, under contract with the National Aeronautics and Space Administration.

Based in part on observations acquired through the Gemini Observatory Archive.

The Pan-STARRS1 Surveys (PS1) and the PS1 public science archive have been made possible through contributions by the Institute for Astronomy, the University of Hawaii, the Pan-STARRS Project Office, the Max-Planck Society and its participating institutes, the Max Planck Institute for Astronomy, Heidelberg, and the Max Planck Institute for Extraterrestrial Physics, Garching, The Johns Hopkins University, Durham University, the University of Edinburgh, the Queen's University Belfast, the Harvard-Smithsonian Center for Astrophysics, the Las Cumbres Observatory Global Telescope Network Incorporated, the National Central University of Taiwan, the Space Telescope Science Institute, the National Aeronautics and Space Administration under Grant No. NNX08AR22G issued through the Planetary Science Division of the NASA Science Mission Directorate, the National Science Foundation Grant No. AST-1238877, the University of Maryland, Eotvos Lorand University (ELTE), the Los Alamos National Laboratory, and the Gordon and Betty Moore Foundation.

IRAF is distributed by the National Optical Astronomy Observatory, which is operated by Universities for Research in Astronomy. This research has made use of National Aeronautics and Space Administration (NASA)'s Astrophysics Data System Bibliographic Services.

REFERENCES

Antezana R. et al., 2013, CBET, 3699
Aretxaga I., Benetti S., Terlevich R. J., Fabian A. C., Cappellaro E., Turatto M., della Valle M., 1999, MNRAS, 309, 343
Benetti S., 2000, Mem. Soc. Astron. Ital., 71, 323
Benetti S., Cappellaro E., Danziger I. J., Turatto M., Patat F., della Valle M., 1998, MNRAS, 294, 448
Benetti S., Turatto M., Cappellaro E., Danziger I. J., Mazzali P. A., 1999, MNRAS, 305, 811
Benetti S. et al., 2016, MNRAS, 456, 3296
Blondin S., Tonry J. L., 2007, in Antonelli L. A., Israel G., Piersanti L., Tornambe A., Burderi L., Di Salvo T., Fiore F., Matt G., Menna M. T., eds, AIP Conf. Proc. Vol. 924, The Multicolored Landscape of Compact Objects and Their Explosive Origins. Am. Inst. Phys., New York, 312
Cappellaro E., 2014, SNOoPY: A Package for SN Photometry. Available at:http://sngroup.oapd.inaf.it/snoopy.html
Cappellaro E., Benetti S., Turatto M., Pastorello A., 2000, Int. Astron. Union Circ., 7380, 2
Cardelli J. A., Clayton G. C., Mathis J. S., 1989, ApJ, 345, 245
Carrasco F. et al., 2013, CBET, 3437
Chambers K. C. et al., 2016, preprint (arXiv:1612.05560)
Chevalier R. A., Fransson C., 1994, ApJ, 420, 268
Chonis T. S., Gaskell C. M., 2008, AJ, 135, 264
Chugai N. N., 1997, Astron. Rep., 41, 672
Chugai N. N., Danziger I. J., 1994, MNRAS, 268, 173
Colas F., Yamaoka H., 2000, Int. Astron. Union Circ., 7378, 1
Crook Aidan C., Huchra John P., Martimbeau N., Masters K. L., Jarrett T., Macri L. M., 2007, ApJ, 655, 790
De Vaucouleurs G., De Vaucouleurs A., Corwin H. G., Buta R. J., Pasturel G., Fouque P., 1991, Third Reference Catalogue of Bright Galaxies (RC3). Springer-Verlag, New York, 9
Elias-Rosa N. et al., 2018, MNRAS, 475, 2614
Fitzpatrick E. L., 1999, PASP, 111, 63
Kitaura F. S., Janka H. T., Hillebrandt W., 2006, A&A, 450, 345
Landolt Arlo U., 1992, AJ, 104, 340
Li W., Filippenko A. V., Van Dyk S. D., Hu J., Qiu Y., Modjaz M., Leonard D. C., 2002, PASP, 114, 403
Magnier E. A. et al., 2016, preprint (arXiv:1612.05240)
Magnier E. A. et al., 2016, preprint(arXiv:1612.05242)
Margutti R. et al., 2014, ApJ, 780, 21
Mauerhan J. C. et al., 2013, MNRAS, 430, 1801
Milisavljevic D., Fesen R. A., Chevalier R. A., Kirshner R. P., Challis P., Turatto M., 2012, ApJ, 751, 25
Moriya T., Tominaga N., Tanaka M., Nomoto K., Sauer D. N., Mazzali P. A., Maeda K., Suzuki T., 2010, ApJ, 719, 1445
Mould J. R. et al., 2000, ApJ, 529, 786
Nomoto K., 1984, ApJ, 277, 791
Pastorello A. et al., 2004, MNRAS, 347, 74
Pastorello A. et al., 2010, MNRAS, 408, 181
Pastorello A. et al., 2013, ApJ, 767, 1
Pastorello A. et al., 2018, MNRAS, 474, 197
Pignata G., Maza J., Hamuy M., Gonzales L., 2009, Rev. Mex. Astron. Astrofis., 35R, 317
Pumo M. L. et al., 2009, ApJ, 705, 138
Reichart D. et al., 2005, NCimC, 28, 767
Schlafly Edward F., Finkbeiner Douglas P., 2011, ApJ, 737, 103
Schlegel E. M., 1990, MNRAS, 244, 269
Shappee B. et al., 2014, A&AS, 2232, 3603
Smith N., 2014, ARA&A, 52, 487
Smith N., Frew D. J., 2011, MNRAS, 415, 2009
Smith N. et al., 2012, MNRAS, 420, 1135
Smith N., Mauerhan J. C., Prieto J. L., 2014, MNRAS, 438, 1191
Smith N. et al., 2017, MNRAS, 466, 3021
Spiro S. et al., 2014, MNRAS, 439, 2873
Stathakis R. A., Sadler E. M., 1991, MNRAS, 250, 786
Tartaglia L. et al., 2016, MNRAS, 459, 1039
Theureau G., Bottinelli L., Coudreau-Durand N., Gouguenheim L., Hallet N., Loulergue M., Paturel G., Teerikorpi G., 1998, A&AS, 130, 333
Theureau G., Hanski M. O., Coudreau N., Hallet N., Martin J. -M., 2007, A&A, 465, 71
Th'one C. C. et al., 2017, A&A, 599, 129
Tomasella L. et al., 2013, MNRAS, 434, 1636
Tonry J. L. et al., 2018, PASP, 130, 064505
Tully R. B., Courtois H. M., Sorce J. G., 2016, AJ, 152, 50
Turatto M., Cappellaro E., Danziger I. J., Benetti S., Gouiffes C., della Valle M., 1993, MNRAS, 262, 128
Utrobin V. P., Chugai N. N., 2011, A&A, 532, 100
Valenti S. et al., 2009, Nature, 459, 674
Valenti S. et al., 2016, MNRAS, 459, 3939
Van Dyk S. D., Filippenko A. V., Peng C. Y., King J. Y., Treffers R. R., Li W., Richmond M. W., 2000, PASP, 112, 1532
Wagner R. M. et al., 2004, PASP, 116, 326
Woosley S. E., Blinnikov S., Heger A., 2007, Nature, 450, 390
Zampieri L., Colpi M., Shapiro S. L., Wasserman I., 1998, ApJ, 505, 876

APPENDIX

A1 Light curves and spectroscopic sequence of SN 2000P

SN 2000P was discovered on 2000 March 8 by the amateur astronomer R. Chassagne at RA = $13^{h}07^{m}09\overset{s}{.}88$ and Dec. = $-28^{\circ}13'59\overset{''}{.}3$ (J2000). The SN was located about 16 arcmin east and 21 arcmin south of the centre of the spiral galaxy NGC 4965 (Colas & Yamaoka 2000). The confirmation image was taken at the Pic du Midi Observatory. The discovery magnitude was 14.1. The original classification as a Type IIn supernova was obtained through an optical spectrum taken on 2000 March 10 with the ESO La Silla 1.54-m Danish telescope + DFOSC (Cappellaro et al. 2000). The redshift of the galaxy and the mean distance modulus, as reported in NED, are $z = 0.007542 \pm 0.000017$ and $\mu = 32.83 \pm 0.77$ mag, respectively.

The *UBVRIJHK* photometry of SN 2000P is presented in Table A1, and the technical information on the spectra is provided in Table A2. In Fig. A1 we give the optical and NIR light curve of SN 2000P, while in Fig. A2 we plot the spectral sequence and the evolution of the Hα profile.

Table A1. Optical and NIR photometric measurements for SN 2000P. For completeness, amateur astronomers' measurements are also included.

Date	MJD	Phase[a]	*U*	*B*	*V*	*R*	*I*	*J*	*H*	*K*	Telescope[b]	Observation PI
2000-03-08	51611.03	0.0				14.10(04)					0.3 m	Chassagne
2000-03-09	51612.12	1.1				14.57(05)					Pic	Colas
2000-03-10	51614.18	3.2	14.31(03)	15.20(02)	15.01(02)	14.76(02)	14.61(02)				Dan	Turatto
2000-03-12	51616.24	5.2	14.68(03)	15.30(02)	15.10(02)	14.86(02)	14.64(02)				Dan	Turatto
2000-03-13	51616.64	5.6			15.17(05)		14.79(05)				0.25 m	Kiyota
2000-03-13	51617.24	6.2	14.91(03)	15.37(02)	15.29(02)	14.94(02)	14.73(02)				Dan	Turatto
2000-04-04	51638.01	27.0			15.30(10)						KAIT	Li et al. (2002)
2000-04-07	51641.08	30.1	15.82(05)	15.98(05)	15.52(02)	15.20(03)	14.98(07)				EF2	Pastorello
2000-04-09	51643.04	32.0			15.67(10)						KAIT	Li et al. (2002)
2000-04-19	51654.00	43.0	17.48(03)	17.60(03)	17.04(03)	16.56(02)	16.39(02)				TNG	Benetti
2000-04-26	51661.25	50.2			17.12(10)						KAIT	Li et al. (2002)
2000-05-23	51687.00	76.0		19.14(05)	18.96(02)	18.37(02)	18.17(05)				TNG	Benetti
2000-05-23	51687.09	76.1						17.55(24)	17.44(21)	16.69(20)	SOFI	Salamanca
2000-05-26	51690.95	79.9								16.64(20)	SOFI	Grosbol
2000-05-27	51691.95	79.9								16.65(12)	SOFI	Grosbol
2000-06-05	51699.50	88.5			19.23(10)						KAIT	Li et al. (2002)
2000-12-06	51884.60	273.6			21.22(02)[c]						*HST*	Li et al. (2002)
2001-02-02	51942.37	331.3	21.65(08)	21.80(09)	21.51(08)	20.56(03)	21.20(06)				EF2	Pastorello
2001-03-17	51985.35	374.3		22.17(10)	21.69(08)	20.62(04)					Dan	Pastorello
2001-03-18	51986.29	375.2					21.26(26)				Dan	Pastorello
2001-04-09	52008.30	397.3						20.57(25)	19.85(30)	19.56(34)	SOFI	Spyromilio
2001-04-12	52012.15	401.1			21.92(12)						Dan	Pastorello
2001-04-23	52022.10	411.1					21.33(03)[d]				*HST*	Li et al. (2002)
2001-07-26	52117.02	506.0		22.49(04)	22.33(05)						VLT1	Cappellaro
2002-08-31	52518.15	907.1				>21.72[e]					EF2	Pastorello
2003-05-20	52779.02	1168.0		24.67(29)	24.10(16)	23.36(11)	22.78(18)				VLT2	Zampieri

Notes. [a]Days from the discovery.
[b]Pic = Gentili 1.05-m Pic du Midi, Dan = ESO Danish 1.54 m+DFOSC, EF2 = ESO 3.6 m+EFOSC2, TNG = TNG 3.6 m+OIG, SOFI = ESO NTT+SOFI, VLT1 = VLT (UT1) 8.2 m+FORS1, VLT2 = VLT (UT4) 8.2 m + FORS2.
[c]*HST* + F555W.
[d]*HST* + F814W.
[e]Upper limit.

Table A2. Spectroscopic observations of SN 2000P.

Date	MJD	Phase[a] (d)	Range (Å)	Resolution[b] (Å)	Telescope	Instrument
2000-03-11	51614.2	3.2	3900–6840	4.7	ESO 1.54 m	DFOSC (gr7)
2000-03-13	51616.3	5.3	3350–9800	9.3	ESO 1.54 m	DFOSC (gr4 + gr5)
2000-03-14	51617.2	6.2	3860–6820	5.1	ESO 1.54 m	DFOSC (gr7)
2000-04-07	51641.1	29.1	3370–9800	16	ESO 3.6 m	EFOSC2 (gr11 + gr12)
2001-02-02	51942.3	331.3	3360–7450	9	ESO 3.6 m	EFOSC2 (gr11)
2001-07-27	52117.0	506.0	4230–8920	11	VLT UT1 8.2 m	FORS1
2003-05-20	52779.0	1168.0	3400–9600	10	VLT UT4 8.2 m	FORS2

Notes. [a]Days from the discovery.
[b]FWHM of the night sky lines.

Table A3. Optical Johnson–Cousins and Sloan photometry of SN 2013gc.

Date	MJD	*B*	*V*	*R*	*I*	*g*	*z*	*y*	Telescope[a]
2010-03-02	55257.32							19.57(0.37)	PS1
2010-04-04	55290.24						20.32(0.15)		PS1
2010-11-02	55517.61						>20.11		PS1
2010-11-17	55517.61							>18.90	PS1
2010-12-24	55554 ± 22			21.78(0.40)					PTF
2011-01-18	55579 ± 1			>20.42					PTF
2011-01-24	55585 ± 3			>18.96					PTF
2011-03-25	55645.24							19.47(0.30)	PS1
2011-10-20	55854.65							19.06(0.16)	PS1
2011-11-14	55879.60						21.06(0.29)		PS1
2012-02-10	55967.37				19.76(0.08)[d]				PS1
2012-04-04	56021.24							>19.72	PS1
2012-10-29	56229.63						20.64(0.31)		PS1
2012-10-30	56230.65							>19.62	PS1
2012-11-14[e]	56245.36			20.89(0.16)[b]	20.99(0.25)[b]				VST
2012-12-28	56289.54				20.19(0.18)[d]				PS1
2013-03-11	56362.28		>18.83						NTT
2013-03-19	56370.16		>19.39						NTT
2013-03-29	56380.98	>18.55	>18.65	>18.44	>18.31				PROMPT
2013-04-01	56383.18	>18.37							PROMPT
2013-04-01	56383.98	>19.21	>18.56	>18.64	>18.13				PROMPT
2013-04-02	56384.14		>20.33						NTT
2013-04-02	56384.98	>18.30	>18.52	>18.13	>17.91				PROMPT
2013-04-04	56386.97	>19.00	>18.76	>18.52	>18.26				PROMPT
2013-04-05	56387.98	>19.95	>18.82		>17.91				PROMPT
2013-04-06	56388.08		>20.58						NTT
2013-04-07	56389.01	>20.01	>19.61						PROMPT
2013-04-08	56390.00	>20.22	>18.84	>19.22	>18.09				PROMPT
2013-04-08	56390.97		>17.58	>17.79	>17.66				PROMPT
2013-04-10	56392.98	>19.71	>18.85	>18.82	>18.26				PROMPT
2013-04-11	56393.97	>18.33							PROMPT
2013-04-12	56394.98	>20.28							PROMPT
2013-04-13	56395.05		>20.35						NTT
2013-04-14	56396.03					>22.37			VST
2013-04-14	56396.04	>18.87	>18.97	>19.28	>18.34				PROMPT
2013-04-14	56396.96	>18.81	>18.00	>18.27					PROMPT
2013-04-16	56398.96	>19.25	>19.56	>19.35	>18.78				PROMPT
2013-04-19	56401.02		>20.29						NTT
2013-04-19	56401.98	>20.99	>20.52	>20.24	>19.72				PROMPT
2013-04-20	56402.96	>20.42	>20.59	>20.58	>19.98				PROMPT
2013-04-22	56404.05	>20.87	>19.09	>19.15	>18.60				PROMPT
2013-04-25	56407.98	>19.42	>19.33	>19.67	>19.25				PROMPT
2013-04-28	56410.08		>17.64						PROMPT
2013-04-28	56410.96		>17.99	>18.34					PROMPT
2013-04-29	56411.96		>18.70						PROMPT
2013-05-01	56413.95	>19.30							PROMPT
2013-05-04	56416.06	>19.64	>18.20						PROMPT
2013-05-04	56416.96			20.45(0.14)					GEMINI

Table A3 – *continued*

Date	MJD	*B*	*V*	*R*	*I*	*g*	*z*	*y*	Telescope[a]
2013-05-05	56417.99	>20.74	>18.84						PROMPT
2013-05-07	56419.01	>20.48	>19.16	>19.07					PROMPT
2013-05-11	56423.96	>20.66	>21.07	>20.43	>20.29				PROMPT
2013-05-15	56427.96	>19.80	>19.99						PROMPT
2013-05-19	56431.96	>19.99	>20.23	>18.71					PROMPT
2013-05-20	56432.97			>20.13	>19.67				PROMPT
2013-05-22	56434.97	>20.90							PROMPT
2013-05-23	56435.96	>19.44	>20.99						PROMPT
2013-05-24	56436.96			>20.12	>19.30				PROMPT
2013-05-29	56441.96	>18.96	>20.13	>20.75	>19.17				PROMPT
2013-06-03	56446.94		>18.15						PROMPT
2013-06-12	56455.95		>19.06	>19.79					PROMPT
2013-06-19	56462.94	>18.23	>18.66						PROMPT
2013-08-26	56530.39			18.21(0.08)					SOAR
2013-09-12	56547.36		15.16(0.02)						NTT
2013-09-13	56548.36		15.14(0.04)						NTT
2013-09-28	56563.38					15.95(0.05)			PROMPT
2013-09-29	56564.40				14.66(0.14)[b]	15.91(0.06)			PROMPT
2013-10-08	56573.29		16.59(0.05)						NTT
2013-11-04	56600.65						16.71(0.02)	16.60(0.03)	PS1
2013-11-06	56602.28	19.93(0.04)	18.75(0.08)						SARA
2013-11-08	56604.30			17.67(0.11)[b]	17.18(0.08)[b]	19.54(0.08)	16.83(0.06)		PROMPT
2013-11-12	56608.31			17.84(0.07)	17.41(0.10)				TRAP
2013-11-16	56612.26			18.29(0.05)	17.53(0.10)				SARA
2013-11-18	56614.25			18.40(0.06)					SOAR
2013-11-26	56622.28	20.86(0.37)	20.04(0.13)						SARA
2013-12-29	56655.17			19.01(0.06)	18.41(0.11)				SARA
2014-01-02	56659.22	21.26(0.12)	20.30(0.04)						TRAP
2014-01-12	56669.19			19.02(0.24)	18.44(0.21)				TRAP
2014-02-02	56690.17			18.96(0.22)	18.49(0.12)				TRAP
2014-02-13	56701.15		20.22(0.19)	18.85(0.05)					TRAP
2014-03-02	56718.11			18.83(0.07)	18.52(0.07)				TRAP
2014-03-22	56738.05				17.38(0.04)				TRAP
2014-04-02	56749.00		19.91(0.09)						TRAP
2014-05-04	56781.24							18.35(0.07)	PS1
2014-05-05	56782.09		19.79(0.11)						PONT
2014-05-08	56785.97	20.59(0.32)	20.18(0.27)	18.64(0.13)	18.41(0.09)				SARA
2014-05-09	56786.99			18.66(0.15)[b]	18.43(0.30)[b]	20.59(0.33)	17.72(0.30)		PROMPT
2014-05-11	56788.98	>20.52	20.09(0.14)	18.68(0.14)	18.38(0.09)				TRAP
2014-05-11	56788.99			18.77(0.06)					SOAR
2014-05-16	56793.98	20.82(0.27)	20.13(0.14)			20.58(0.23)			SARA
2014-05-27	56804.96	20.54(0.33)	19.93(0.20)	19.04(0.13)	18.52(0.10)				SARA
2014-05-30	56807.98	20.91(0.16)	19.83(0.10)	18.56(0.08)					SMARTS
2014-06-01	56809.97	20.88(0.18)	20.01(0.13)	18.67(0.11)	18.18(0.20)				TRAP
2014-06-10	56818.97	>20.93							TRAP
2014-06-26	56834.97			19.28(0.19)	18.84(0.23)				SARA
2015-02-22	57075.05	>21.01	>21.00		>19.46				TRAP
2015-04-02	57114.02	>21.21	>20.94	20.84(0.46)	>20.34				TRAP
2015-05-01	57143.99	>20.45	>20.54	20.95(0.32)	>19.93				TRAP
2015-05-12	57154.00	>21.26							TRAP
2015-05-20	57163.00			21.04(0.18)	>20.13				TRAP
2015-06-01	57174.99	>20.37	>20.26	21.18(0.37)	>20.12				TRAP
2015-06-11	57185.00	>20.78							TRAP
2017-03-04[c]	57816 ± 47					23.57(0.22)	22.62(0.24)		DEC

Notes. [a]NTT = ESO 3.6-m NTT+EFOSC2, SOAR = 4.1-m 'SOAR'+Goodman Spectrograph, TRAP = 0.5-m TRAPPIST, SMARTS = CTIO 1.3 m+ANDICAM, SARA = CTIO 0.6 m+ARC, GEMINI = 8.1-m Gemini-South+GMOS-S, PTF = 1.2-m 'S. Oschin' Schmidt+PTF survey, PONT = Las Campanas 2.5-m 'Du Pont'+WFCCD/WF4K-1, PS1 = Haleakala 1.8 m+Pan-STARRS1 Survey, DEC = CTIO 4-m 'V. Blanco' + Dark Energy Camera (DECaPS survey).

[b]Converted from Sloan to Johnson photometric system.

[c]For this epoch we also report $r = 22.63(0.18)$.

[d]PS1 *i*-band magnitude, not converted to *I*.

[e]For this epoch and this instrument we also report $u > 21.40$.

Table A4. NIR photometry of SN 2013gc.

Date	MJD	*J*	*H*	*K*	Telescope[a]
2013-03-18	56370.00	>19.70	>18.02	>18.32	SOFI
2013-04-04	56386.02	19.29(0.33)	18.84(0.32)	18.08(0.19)	SOFI
2013-04-12	56394.05	19.39(0.26)	18.74(0.40)	17.91(0.25)	SOFI
2013-04-18	56400.05	19.46(0.27)	18.81(0.33)	18.54(0.37)	SOFI
2014-05-30	56807.98	17.29(0.16)	17.15(0.18)	17.55(0.30)	SMARTS

Note. [a]SOFI = ESO 3.6-m NTT+SOFI, SMARTS = CTIO 1.3 m + ANDICAM.

Table A5. Clear photometry of SN 2013gc, treated as *R*-band.

Date	MJD	Clear	Telescope
2011-01-27	55588.07	>18.99	PROMPT
2011-02-01	55593.08	>19.32	PROMPT
2011-02-20	55612.10	>19.72	PROMPT
2011-03-06	55626.06	19.70(0.15)	PROMPT
2011-03-12	55632.03	>19.68	PROMPT
2011-05-02	55683.08	>19.57	PROMPT
2011-09-14	55818.37	>19.01	PROMPT
2011-09-25	55829.34	>19.57	PROMPT
2011-10-17	55851.28	>19.08	PROMPT
2011-10-22	55856.35	>18.49	PROMPT
2011-11-02	55867.24	>19.47	PROMPT
2012-01-04	55930.10	>19.16	PROMPT
2012-01-07	55933.19	20.36(0.36)	PROMPT
2012-01-10	55936.20	>19.27	PROMPT
2012-01-14	55940.21	20.42(0.27)	PROMPT
2012-01-18	55944.18	>20.01	PROMPT
2012-01-24	55950.15	>19.95	PROMPT
2012-01-27	55953.15	20.46(0.41)	PROMPT
2012-01-29	55955.13	>19.72	PROMPT
2012-02-01	55958.20	20.93(0.41)	PROMPT
2012-02-03	55960.16	>19.48	PROMPT
2012-02-06	55963.12	>19.57	PROMPT
2012-02-08	55965.14	19.89(0.45)	PROMPT
2012-02-10	55967.11	19.93(0.37)	PROMPT
2012-02-12	55969.10	20.35(0.34)	PROMPT
2012-02-21	55978.10	>20.16	PROMPT
2012-02-24	55981.07	>19.39	PROMPT
2012-02-25	55982.09	21.09(0.50)	PROMPT
2012-02-26	55983.08	20.00(0.20)	PROMPT
2012-02-27	55984.09	20.65(0.26)	PROMPT
2012-03-02	55988.09	>19.64	PROMPT
2012-03-05	55991.07	>19.90	PROMPT
2012-03-07	55993.05	>19.19	PROMPT
2012-03-09	55995.07	19.96(0.37)	PROMPT
2012-03-11	55997.06	>19.26	PROMPT
2012-03-13	55999.05	>19.95	PROMPT
2012-03-14	56000.06	>18.70	PROMPT
2012-03-16	56002.05	21.27(0.46)	PROMPT
2012-03-18	56004.04	>20.14	PROMPT
2012-03-26	56012.03	>20.12	PROMPT
2012-03-31	56017.01	20.29(0.47)	PROMPT
2012-04-06	56023.01	>19.63	PROMPT
2012-10-11	56211.30	>19.67	PROMPT
2012-10-14	56214.29	>19.71	PROMPT
2012-11-27	56258.22	>19.72	PROMPT
2012-12-01	56262.25	19.93(0.32)	PROMPT
2012-12-04	56265.30	>19.43	PROMPT
2012-12-06	56267.29	>19.75	PROMPT
2012-12-09	56270.15	>19.09	PROMPT
2012-12-13	56274.20	>19.86	PROMPT
2012-12-16	56277.12	>19.80	PROMPT
2012-12-21	56282.12	20.47(0.42)	PROMPT
2012-12-24	56285.16	20.41(0.39)	PROMPT

Table A5 – *continued*

Date	MJD	Clear	Telescope
2012-12-27	56288.23	20.10(0.44)	PROMPT
2012-12-31	56292.22	>19.69	PROMPT
2013-01-04	56296.21	>19.48	PROMPT
2013-01-13	56305.22	>19.62	PROMPT
2013-01-16	56308.12	>19.69	PROMPT
2013-01-23	56315.35	>19.36	PROMPT
2013-01-26	56318.14	>19.37	PROMPT
2013-02-02	56325.21	>19.56	PROMPT
2013-02-08	56331.30	>19.62	PROMPT
2013-02-15	56338.15	>20.02	PROMPT
2013-03-09	56360.23	>19.79	PROMPT
2013-03-10	56361.12	>19.50	PROMPT
2013-03-11	56362.14	>19.01	PROMPT
2013-03-17	56368.08	>19.71	PROMPT
2013-03-19	56370.22	>19.52	PROMPT
2013-03-23	56374.18	>19.21	PROMPT
2013-03-26	56377.18	>19.25	PROMPT
2013-03-28	56379.12	>19.58	PROMPT
2013-04-04	56386.07	>19.51	PROMPT
2013-04-21	56403.03	>19.69	PROMPT
2013-11-07	56603.33	17.59(0.08)	PROMPT
2013-11-08	56604.25	17.78(0.07)	PROMPT
2013-11-09	56605.23	17.77(0.08)	PROMPT
2013-11-11	56607.22	17.83(0.06)	PROMPT
2013-11-14	56610.21	18.15(0.14)	PROMPT
2013-11-17	56613.27	18.31(0.15)	PROMPT
2013-11-19	56615.24	18.52(0.13)	PROMPT
2013-11-21	56617.19	19.06(0.15)	PROMPT
2013-11-24	56620.31	19.10(0.18)	PROMPT
2013-11-26	56622.28	19.08(0.13)	PROMPT
2013-11-30	56626.20	19.14(0.18)	PROMPT
2013-12-02	56628.16	19.16(0.17)	PROMPT
2013-12-06	56632.15	19.19(0.20)	PROMPT
2013-12-12	56638.14	19.29(0.13)	PROMPT
2014-03-12	56728.21	18.21(0.11)	PROMPT
2014-04-10	56757.09	18.13(0.07)	PROMPT
2014-04-11	56758.14	18.34(0.10)	PROMPT
2014-04-16	56763.08	18.50(0.19)	PROMPT
2014-04-17	56764.08	18.70(0.15)	PROMPT
2014-04-19	56766.06	18.61(0.08)	PROMPT
2014-04-20	56767.09	18.77(0.11)	PROMPT
2014-04-22	56769.07	18.64(0.06)	PROMPT
2014-05-13	56790.05	19.14(0.17)	PROMPT
2014-05-16	56793.00	19.07(0.10)	PROMPT
2014-09-07	56907.40	19.99(0.38)	PROMPT
2014-09-24	56924.36	20.05(0.37)	PROMPT
2014-10-03	56933.37	20.11(0.41)	PROMPT
2014-10-09	56939.31	>18.21	PROMPT
2014-10-11	56941.30	>18.47	PROMPT
2014-10-20	56950.28	20.28(0.33)	PROMPT
2014-11-08	56969.22	>18.99	PROMPT
2014-11-13	56974.32	>19.80	PROMPT
2015-01-03	57025.20	>19.54	PROMPT
2015-01-07	57029.19	>19.41	PROMPT

Table A5 *– continued*

Date	MJD	Clear	Telescope
2015-01-10	57032.34	>19.98	PROMPT
2015-01-12	57034.26	>19.98	PROMPT
2015-01-14	57036.31	20.30(0.32)	PROMPT
2015-01-16	57038.29	>20.02	PROMPT
2015-01-21	57043.34	20.38(0.37)	PROMPT
2015-01-22	57044.26	>19.18	PROMPT
2015-01-26	57048.32	>19.79	PROMPT
2015-01-27	57049.26	20.19(0.36)	PROMPT
2015-01-29	57051.28	20.13(0.36)	PROMPT
2015-02-01	57054.26	>19.62	PROMPT
2015-02-03	57056.33	>18.71	PROMPT
2015-02-04	57057.27	>18.60	PROMPT
2015-02-07	57060.15	>19.58	PROMPT
2015-02-08	57061.30	>19.00	PROMPT
2015-02-10	57063.10	>19.64	PROMPT
2015-02-12	57065.22	20.36(0.25)	PROMPT
2015-02-17	57070.30	>19.75	PROMPT
2015-02-18	57071.30	>19.83	PROMPT
2015-02-22	57075.09	>19.78	PROMPT
2015-02-24	57077.09	20.41(0.30)	PROMPT
2015-02-26	57079.27	>18.96	PROMPT
2015-03-06	57087.08	>19.07	PROMPT
2015-03-12	57093.14	>19.71	PROMPT
2015-03-14	57095.18	20.49(0.33)	PROMPT
2015-03-18	57099.22	>19.08	PROMPT
2015-03-28	57109.19	>19.06	PROMPT
2015-03-30	57111.17	>19.02	PROMPT
2015-04-04	57116.04	>19.15	PROMPT
2015-04-11	57123.12	>19.14	PROMPT

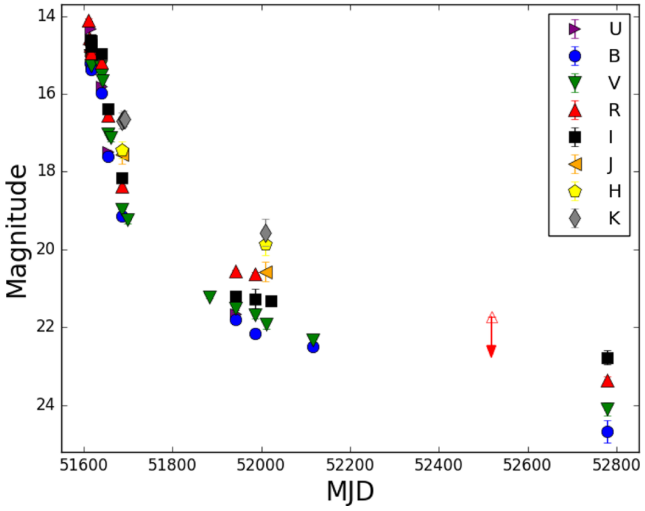

Figure A1. Optical and NIR light curves of SN 2000P, spanning about three years of observations. The magnitudes are not corrected for line-of-sight extinction. The red arrow indicates an upper limit in the *R* band.

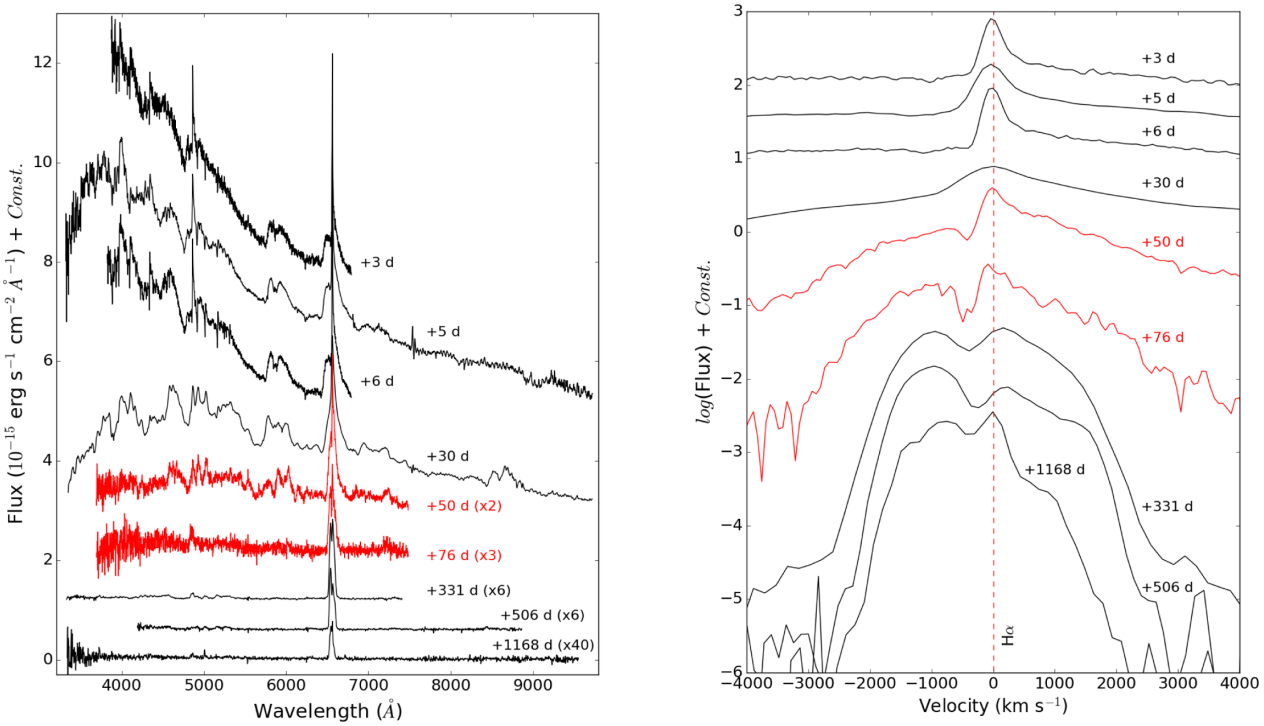

Figure A2. Left: time sequence of optical spectra of SN 2000P, spanning about three years of observations. The fluxes of the spectra are scaled to the *R*-band or, if not available, to the *V*-band photometry of the nearest night. The spectra plotted in red colour are taken from the CfA Supernova Data Archive (https://www.cfa.harvard.edu/supernova/SNarchive.html), to fill the time gap of our sequence. Right: evolution of the H α profile in the same spectral sequence. The logarithm of the specific flux is reported on the *y*-axis. The velocity with respect to the rest frame is shown. In both graphs, the phase is relative to the discovery.

This paper has been typeset from a TEX/LATEX file prepared by the author.